OXFORD

Journal of Petrology, 2023, 0–23
https://doi.org/10.1093/petrology/egad038
Original Manuscript

Melt Inclusions in Arclogitic Xenoliths Constrain the Genesis of the Lower Continental Arc Crust beneath the Northern Volcanic Zone, Colombia

Omar Gianola [1,*], Benedetta Costa [1,†], Fabio Ferri [1], Mattia Gilio [2], Maurizio Petrelli [3], Mara Murri [2], Anna Barbaro [1], Matteo Alvaro [2], Andrés Rodríguez-Vargas [4], Stefano Poli [5] and Bernardo Cesare [1]

[1]Department of Geosciences, University of Padova, Via G. Gradenigo 6, 35131 Padova, Italy
[2]Department of Earth and Environmental Sciences, University of Pavia, Via A. Ferrata 1, 27100 Pavia, Italy
[3]Department of Physics and Geology, University of Perugia, Piazza dell'Università, 06123 Perugia, Italy
[4]Minerlab Limitada, Calle 51 Sur No 80i-34, Bogotá, DC., Colombia
[5]Dipartimento di Scienze della Terra "Ardito Desio", Università degli Studi di Milano, Via Mangiagalli 34, 20133, Milano, Italy

*Corresponding author. E-mail: gianola@snsb.de
†Present address: Institute of Material Technology, Building Physics and Building Ecology, Faculty of Civil Engineering, Vienna University of Technology (TU Wien), Karlsplatz 13/207-01, A-1040 Vienna, Austria

AQ8

Abstract

Volcanic arcs above subduction zones are thought to be the principal locations where juvenile magmatic crust forms and is refined to become continental crust with an andesitic composition. During this refinement mechanism, the formation of dense garnet pyroxenites (arclogites), represented by high-pressure cumulates and restites after partial melting, leads to the delamination of the lower arc crust. The Mercaderes-Río Mayo area in southern Colombia is the only known locality in an active volcanic arc where arclogitic xenoliths have been recovered. These xenoliths are entrained in the Granatifera Tuff, a late Cenozoic volcanic vent, and they mainly consist of garnet, clinopyroxene, amphibole, plagioclase, rarely scapolite, and accessory mineral inclusions of rutile, apatite, zircons, and quartz. Moreover, the arclogites are also characterized by the presence of melt inclusions (MI), which are mainly found within garnet, but can be also observed in amphibole, plagioclase, clinopyroxene, and scapolite. The glasses measured for the MI in garnet and scapolite typically have SiO_2 contents >57 wt.%, ranging from andesite to rhyolite in composition. Petrographic and geochemical investigations allowed to discriminate between cumulitic and restitic arclogites, with the latter showing the concomitant presence of primary MI and quartz inclusions within the peritectic garnets. Therefore, our study provides for the first time a strong evidence, at the microscale, for the anatectic origin of some arclogitic xenoliths. Pressure and temperature conditions for the studied arclogites were estimated by intracrystalline geothermometry, elastic geothermobarometry, phase equilibria modelling and classical Fe–Mg exchange between garnet and clinopyroxene. Results mainly fall within the range of 960°C to 1150°C and 1.6 to 1.9 GPa for most samples. We suggest that the investigated arclogites derive from the root of the active Colombian volcanic arc, where differentiation processes from mantle-derived melts and lower crust anatexis occur in close association.

Keywords: subduction, elastic geothermobarometry, crustal growth, arc root, Andean volcanism

INTRODUCTION

Active volcanic arcs, both oceanic and continental, are the direct result of crustal recycling along subduction zones. The devolatilization of dense subducting oceanic slabs lowers the solidus of the overlying peridotitic mantle and triggers the production of predominantly basaltic magmas, which chemically differentiate along their ascending paths and eventually erupt at the surface. With an overall length of ~41 000 km (Schmidt & Poli, 2013), modern active volcanic arcs contribute significantly to the formation of juvenile continental crust. There is indeed sound evidence that the average composition of plutonic and volcanic rocks generated in many volcanic arcs resembles the average composition of the continental crust (Rudnick, 1995; Taylor & McLennan, 1995; Jagoutz & Schmidt, 2012), highlighting the pivotal role played by arc magmatic processes in the formation of modern continental crust. Despite this gross similarity, it has been noticed that the chemical composition of the lower arc crust largely differs from that of continents at comparable depths (Jagoutz & Behn, 2013; Hacker *et al.*, 2015; Kelemen & Behn, 2016) and, therefore, some refinement mechanisms are necessary to transform arc crust into the continental crust. The two most accredited processes responsible for the lower arc crust refinement are thought to be delamination of dense arc rocks and relamination of more buoyant material from the subduction zone. Relamination is inferred to take place in different ways, and principally, it might involve the emplacement of less dense material at the base of the arc crust. This less dense material may have different origins and compositions, including subducted sediments, subducted intra-oceanic arc sections, portions of crust removed from the overriding plate or subducted continental crust (e.g. Hacker *et al.*, 2011; Kelemen & Behn, 2016). By contrast, delamination is a density sorting effect in which dense magmatic

Received: December 30, 2022. **Revised:** April 16, 2023. **Accepted:** May 21, 2023

arc cumulates or granulite- to eclogite-facies metamorphosed arc lithologies become gravitationally unstable and sink into the underlying mantle (e.g. Jagoutz & Schmidt, 2013; Jagoutz & Kelemen, 2015). The delaminating rocks mainly consist of garnet, pyroxene, amphibole, and Fe–Ti oxides and are often grouped under the descriptive name of arclogites (Lee & Anderson, 2015; Ducea *et al.*, 2021a). The twofold origin (cumulate vs. restite) of arclogitic assemblages is extensively debated (Tatsumi, 2000; Lee *et al.*, 2006; Ducea *et al.*, 2021a), and there are no unequivocal criteria for its assessment. Determining the chemical composition and structure of the lower arc crust is not an easy task since few locations in the world offer an adequate exposure of tilted arc roots. Among these, particularly relevant are the Kohistan (N-Pakistan; e.g. Garrido *et al.*, 2006; Burg, 2011; Jagoutz & Schmidt, 2012) and the Talkeetna (S-Alaska; e.g. Greene *et al.*, 2006; DeBari & Greene, 2011; Kelemen *et al.*, 2014) paleo-arcs, as archetypes for intra-oceanic arcs, and the southern Sierra Nevada (W-USA; e.g. Saleeby, 1990; Klein & Jagoutz, 2021) and the Sierra de Valle Fértil (W-Argentina; e.g. Otamendi *et al.*, 2012; Ducea *et al.*, 2015), as examples of continental arc sections. Additional knowledge can also be acquired by the study of mafic (i.e. 'arclogitic') and felsic xenoliths entrained in volcanic rocks. Although xenoliths tell little about the structure of the lower arc edifice, they are not affected by metamorphic re-equilibration due to late tectonic events and hence they provide invaluable information on the mineral assemblage and chemical composition of the lower arc crust. Several localities worldwide host lower arc crustal xenoliths (e.g. Ducea *et al.*, 2021a) but one of them, the Mercaderes-Río Mayo area in SW Colombia, is of particular interest because it is the only known location where lower crustal xenoliths derive from an active Andean-type arc (Weber *et al.*, 2002; Rodríguez-Vargas *et al.*, 2005; Bloch *et al.*, 2017). In this area, volcanic tuffs contain mantle and crustal xenoliths, allowing to probe and investigate the entire column above the down-going oceanic slab.

In this study, we focus on some crustal xenoliths recovered from the Mercaderes-Río Mayo area, as they provide unique clues to the differentiation and re-working processes that characterize the root of an active continental arc. Melt inclusions hosted in their rock-forming minerals (in particular garnet) helped to constrain the origin of these arclogites, some of which are interpreted as restites, whereas elastic thermobarometry allowed to establish the depths and temperatures at which the xenoliths resided before being incorporated in the ascending magma. We also provide evidence that growth and 'maturation' of a lower arc root are determined by the interplay between fractional crystallization from mantle-derived melts and partial melting of crustal metabasaltic precursors.

GEOLOGICAL SETTING

The Andean Cordillera is a subduction-related active volcanic chain that can be subdivided, from south to north, into four distinct zones, the Austral Volcanic Zone, the Southern Volcanic Zone, the Central Volcanic Zone, and the Northern Volcanic Zone (NVZ). The NVZ comprises the modern active-arc section located between central Ecuador and central Colombia, approximately from 1°S to 7°N, and is bounded by the Colombian flat slab to the north and the Peruvian flat slab to the south (Syracuse *et al.*, 2016).

The Colombian territory can then be divided into three parallel Cordilleras elongated approximately NE–SW, the Western, the Central, and the Eastern Cordillera, produced by superposition of multiple orogenic events occurring since the Palaeozoic to the present. The Western Cordillera has an oceanic affinity and is separated from the Central and Eastern Cordilleras, both with a continental affinity, by the Romeral Fault System (RFS). The latter, in the area of investigation, is identified as the Cauca–Almaguer fault and possibly represents a subduction zone of continental-ocean type, which was blocked by the thick, buoyant plateau, enabling subduction to migrate once more to the west. Few episodes of crustal growth occurred with the generation of igneous bodies from the Jurassic to the Neogene (Taboada *et al.*, 2000). Seismic investigations with V_p and V_s have shown that in the Mercaderes-Río Mayo area the crustal thickness ranges between 50 and 70 km, with an arc root that possibly is 13 to 20 km thick (Poveda *et al.*, 2015; Avellaneda-Jiménez & Monsalve, 2022).

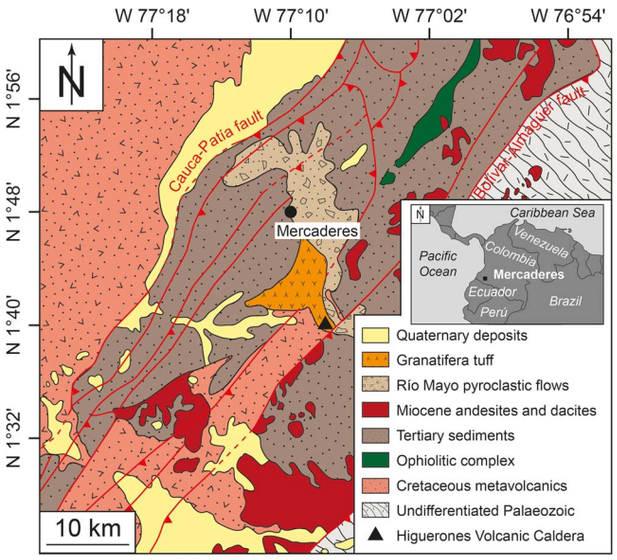

Fig. 1. Tectonic map of the Mercaderes area (modified after Weber *et al.*, 2002 and Rodríguez-Vargas *et al.*, 2005). Coordinates are given according to WGS84.

The Mercaderes–Río Mayo area carries the famous lower crustal and mantle xenoliths recovered within the Granatifera tuff formation. This area (Fig. 1) is characterized by a complex lithologic sequence including metasedimentary rocks of the paleozoic Arquía Complex; metavolcanis and metasedimentary units of the Cretaceous Diabásico Group; sedimentary rocks of the Mosquera–Esmita Formation and pyroclastic rocks of the Galeón Formation with tertiary-quaternary age. All these units were intruded by the tertiary porphyritic volcanics of dacitic and andesitic composition (Murcia & Cepeda, 1991; Weber, 1998). The metasediments and metavolcanics are in turn capped by the ~300-m-thick Granatifera Tuff, which is thought to represent an eroded tuff cone or tuff ring (Weber *et al.*, 2002). Rodríguez-Vargas *et al.* (2005) suggested that the emission vent of the Granatifera Tuff is reasonably located few hundred meters from the village of Higuerones, where the volcanic edifice is partly preserved in the form of a caldera.

The Granatifera Tuff is divided into three main parts with the basal section composed of volcanic breccias, agglomerates and lapilli tuffs, overlain by lithified tuffs, ash deposits and debris flows (Weber *et al.*, 2002; Rodríguez-Vargas *et al.*, 2005).

The crustal and mantle xenoliths within the Granatifera Tuff are up to 20 cm in diameter and include garnet-bearing rocks ranging from peridotites to websterites as most common mantle xenoliths, garnet-free websterites and minor amounts of

spinel-bearing mantle xenoliths. The lower crustal xenoliths comprise a variety of amphibolites, pyroxenites, granulites, and gneisses, metamorphosed under amphibolite to granulite facies conditions. According to Lu-Hf dating, the xenoliths are younger than 5 Ma and may represent fragments of the lowermost arc root and the underlying mantle wedge (Bloch *et al.*, 2017).

ANALYTICAL METHODS

Back-scattered electron (BSE) images and semi-quantitative energy dispersive spectroscopy (EDS) analyses of melt inclusions (MI) were carried out with a CamScan MX2500 Scanning Electron Microscope (SEM), at the Department of Geosciences of the University of Padova (Italy) and with a FEI Quanta 200 at CEASC (Centro di Analisi e Servizi per la Certificazione, University of Padova).

Major element compositions of glasses and minerals were determined with a JEOL JXA-8200 Superprobe electron probe micro-analyser (EPMA), equipped with five wavelength dispersive spectrometers, at the Department of Earth Sciences (University of Milano, Italy), employing an acceleration voltage of 15 kV, a beam current of 5 or 15 nA and beam diameter of 1 μm (enlarged up to 10 μm for some analyses). Acquisition times were 10 seconds on peak and 5 seconds for background, measuring Na and K first to minimize diffusional losses. Natural and synthetic minerals and glasses from the Smithsonian Microbeam Standards (Jarosewich *et al.*, 1980; Jarosewich, 2002) and from Ingamells (1978) were used as elemental standards and to monitor the analytical reproducibility. Si and Ca were measured on grossular, Mg on olivine, Al on anorthite, Ti on ilmenite, Mn on rhodonite, Fe on fayalite, Cr on pure chromium, Na on omphacite, K on K-feldspar, P on a Y-phosphate and S on celestine. For glasses analysed in the xenoliths, alkali concentrations were corrected using conservative factors obtained by the analysis of hydrous and anhydrous leucogranitic glasses of known composition. In this study we employed a 10.1 wt.% H_2O-bearing glass (LGB 2; Behrens & Jantos, 2001), a 5.5 wt.% H_2O-bearing glass (DL; Acosta-Vigil *et al.*, 2003) and a nearly anhydrous ($H_2O = 300 \pm 42$ μg/g, 2 s.e.m.) glass (B; Morgan & London, 2005). Glass and mineral standards are reported in Supplementary Table S1.

Laser ablation inductively coupled mass spectrometer (LA-ICP-MS) measurements of trace elements in glasses were performed at the Department of Physics and Geology, University of Perugia (Italy) using a Teledyne Photon Machine G2 laser ablation device coupled to a Thermo Fischer Scientific iCAP Q quadrupole mass spectrometer. Trace element concentrations in the unknowns were calibrated against NIST SRM 610 as external standard and the USGS BCR2G reference material was processed as an unknown to assess the quality of the measurements and the accuracy of the calculations. Under the reported analytical conditions, precision and accuracy values are typically below 10% (Petrelli *et al.*, 2016a, 2016b). Analyses were conducted using a classical sample-standard bracketing, where NIST SRM 610 was measured twice every 12 to 15 samples. Both standard and unknowns were ablated using a circular spot with a diameter of 15 μm (except for one sample where a spot size of 25 μm was employed), a repetition rate of 10 Hz and an energy density of 3 to 4 J/cm^2. Ablation times were 30 seconds per spot, preceded by a 30-second background measurement and followed by 20 seconds of washout. Si was used as internal standard and measured intensities were then converted into concentrations using the Iolite 3 software (Paton *et al.*, 2011). Conservatively, elements that are strongly enriched in the host garnet (heavy rare earth elements, Y, Sc, V, and Mn) were not considered for the analysed glasses of the melt inclusions, in order to avoid any artefact value that may derive from the possible mixed analysis with the host. The complete trace elements data set can be found in Supplementary Table S2.

Raman spectra of quartz and zircon inclusions in garnet were measured at the University of Pavia with a Horiba LabRam HR Evolution spectrometer (holographic gratings of 1800 grooves/mm) equipped with an Olympus BX41 confocal microscope at controlled temperature of 20 ± 1°C. Raman spectra were excited using the 532 nm line of a solid state (YAG) laser. The laser power on the sample surface was approximately 1 to 2 mW. The spectrometer was calibrated to the Raman peak of silicon at 520.5 cm^{-1}. We used spectra of free crystals with the same composition as the inclusions as further calibration for the entire spectral range used in our investigation. The collected spectra were baseline-corrected for the continuum luminescence background when necessary, temperature-reduced to account for the Bose-Einstein occupation factor (Kuzmany, 2009) and normalized to the acquisition time. Peak positions, full widths at half maximum (FWHMs), and integrated intensities were assessed from fits with pseudo-Voigt functions. For each of the selected Raman bands we determined the shift $\Delta\omega$ of the Raman band as the difference between the Raman shift of the inclusion ω_i from that of an unstrained reference crystal (ω_0). As standards, we used free (unstrained) quartz (mineralogical collection University of Pavia) and zircon (Mud Tank Hill, Australia) crystals, measured multiple times during each measurement session at ambient pressure and room temperature to eliminate shifts in peak positions due to instrumental drift and/or minor changes in room temperature. The ω_0 values were averaged and then subtracted from the ω_i of the strained inclusions analysed in between two consecutive standard measurements. For zircon inclusions, because of the possible misinterpretations due to effects of radiation damages (which change the elastic properties of zircon causing shifting and broadening of the Raman peaks, Binvignat *et al.*, 2018), we adopted the procedure described in Campomenosi *et al.* (2020). Therefore, we included in the analysis only inclusions with full widths at half-maximum (FWHM) for the 1014 Raman band smaller than $\omega_{1014}^{FWHM} < 5.0\ cm^{-1}$. The $\Delta\omega$ values of each mode of zircon and quartz inclusions and unstrained standards are listed in the supplementary material (Supplementary Table S3). Finally, sets of $\Delta\omega$ for each inclusion (modes ω_{128}, ω_{206}, ω_{265}, and ω_{464} for quartz and modes ω_{438}, ω_{969}, ω_{1014} for zircon, as they are generally unaffected by overlap with modes of the host garnet and have no significant shifts due to changes in composition) have been used to determine strain using the software stRAinMAN (Angel *et al.*, 2019) by employing the Grüneisen tensors for quartz (Murri *et al.*, 2018a) and zircon (Stangarone *et al.*, 2019). The differences of the thermoelastic properties of a host–inclusion pair system may lead to the development of residual pressures upon exhumation (Rosenfeld & Chase, 1961; Angel *et al.*, 2014). Knowing the inclusion pressure (P_{inc}) at T_0 (25°C) and the thermodynamic properties of host and inclusion one can back-calculate a line of possible entrapment conditions in the P–T space: the isomeke (Rosenfeld & Chase, 1961; Angel *et al.*, 2014; Angel *et al.*, 2017b). The entrapment isomekes for quartz and zircon inclusions were obtained from the strains with the software EntraPT (Mazzucchelli *et al.*, 2021), using the equation of state of quartz (Angel *et al.*, 2017a), zircon (Ehlers *et al.*, 2022), and garnet end-members (Angel *et al.*, 2022). The isomekes were then corrected for garnet composition following the method described in Angel *et al.* (2022). The strain of each inclusion was converted to stress using the elastic tensors at room P–T for quartz (Wang *et al.*, 2015) and zircon

(Özkan *et al.*, 1974). The P_{inc} was calculated from the stress tensor as the mean normal stress ($P_{inc} = (\sigma_1 + \sigma_2 + \sigma_3)/3$). The uncertainty on P_{inc} of each inclusion was propagated from the uncertainty on strain using the respective elastic tensor by the software EntraPT, through the procedure described in Mazzucchelli *et al.* (2021). To avoid the effects of strain localization at corners and inclusion shape effects (Mazzucchelli *et al.*, 2018; Campomenosi *et al.*, 2020), each Raman measurement was performed at the center of well-rounded quartz and zircon inclusions.

Single-crystal X-ray diffraction data collections, followed by structural refinements with chemical constraints, were carried out on seven pyroxene single crystals from the sample 18XC10 in order to determine the closure temperatures related to the Fe^{2+}–Mg exchange reaction (Ganguly, 1982). X-ray diffraction data collections have been carried out using a Rigaku-Oxford Diffraction Supernova diffractometer available at the Department of Geosciences, University of Padova. The instrument is a kappa-geometry goniometer equipped with an X-ray microsource, MoK_α ($\lambda = 0.71073$ Å) operating at 50 kV and 0.8 mA (power = 40 W) and a Pilatus 200K Dectris area detector. Data collections and data reduction, including intensity integration together with background and Lorentz-polarization corrections, have been performed using the Crysalis software (Rigaku-Oxford-Diffraction©) package. The unit-cell parameters with the discrepancy indices R_{int}, R_{all}, R_w on all the observed structure factors (F_o^2) and the goodness of fit (*S*) of the structure refinements with chemical constraints for the seven crystals are reported in Supplementary Table S4 together with the mean atomic numbers (m.a.n.) in electrons per formula unit (e.p.f.u.) at the crystallographic sites (*M*1, *M*2, *M*21) obtained when the structure refinement reached convergence, before introducing the chemical constraints. For all samples the calculated mean atomic numbers from the unconstrained refinements agree within two standard deviations with the values of electrons per formula unit (e.p.f.u.) calculated from the EPMA (Supplementary Table S4). Therefore, this enabled us to use the results from the EPMA as chemical constraints for the structural refinements, following the procedure and taking into account the same constraints as in Domeneghetti *et al.* (2013), to determine the clinopyroxene site distribution (assuming one standard deviation as the error). The structure refinements with chemical constraints have been carried out following the procedure reported in Murri *et al.* (2018b) and Murri *et al.* (2019) by using the SHELX-97 program (Sheldrick, 2008). The site populations obtained from the structural refinements with chemical constraints and the distribution coefficients (k_D), with their relative errors, are reported in the Supplementary Table S4. Errors on k_D were calculated by standard error propagation.

The P–T conditions for sample 18XC10 were also investigated by phase equilibria modelling for the chemical systems CaNaKFMASHTiMn. The bulk rock composition was estimated by combining the modal mineral proportions obtained from a compositional SEM map and the mineral compositions measured by EPMA (see below). Due to the nearly dry nature of the rock, it has been assumed that the only source of water was amphibole and, therefore, calculations were performed with a H_2O content of 0.04 wt.%. Stability fields of coexisting minerals were outlined by Gibbs free energy minimization using the Perple_X software package (version 6.9.1; Connolly, 2005, 2009). Calculations take into account solution models for the following phases: clinopyroxene, amphibole and melt (Green *et al.*, 2016), garnet and orthopyroxene (White *et al.*, 2014), feldspar (Holland & Powell, 2003), spinel (White *et al.*, 2002) and ilmenite (White *et al.*, 2000).

RESULTS

Mineral assemblages

We studied four samples, 3 to 5 cm in size, representative of the crustal xenoliths: 18XC1, 18XC5, 18XC10 and 18XC20 (Supplementary Fig. S1a–d). They broadly encompass the categories of Grt-Px hornblendites (mineral abbreviations after Whitney & Evans, 2010), pyribolites and pyroxenites as defined by Weber *et al.* (2002) and can also be collectively defined as arclogites according to the criteria of Ducea *et al.* (2021a).

Sample 18XC1 contains, in order of decreasing abundance, garnet, plagioclase, amphibole, clinopyroxene and rare scapolite. The texture is slightly layered, inequigranular interlobate, with an average grain size of 1 to 2 mm, where rare garnet crystals may reach 7 mm. All grain boundaries display evidence of reaction between adjacent minerals and of infiltration of external melt (Fig. 2a). In some cases, the minerals may be intensely altered or transformed (e.g. pyroxene into amphibole). In places, subhedral crystals of plagioclase with planar crystal faces (Fig. 2b) indicate crystallization from a melt (Sawyer, 2008). Melt inclusions have been observed in garnet and in the cores ofplagioclase. The modal composition for 18XC1, determined through a SEM compositional map from a thick section (see Supplementary Fig. S2a), is as follows: 36.1 vol.% garnet, 12.4 vol.% clinopyroxene, 27.0 vol.% plagioclase, 22.8 vol.% amphibole, 1.3 vol.% scapolite, 0.2 vol.% apatite and 0.1 vol.% rutile.

Sample 18XC5 consists of garnet, amphibole, clinopyroxene and rare plagioclase and scapolite. It has an isotropic granoblastic microstructure where the coarser mineral, anhedral garnet, may reach 4 mm in size (Supplementary Fig. S1b). Microstructural relationships suggest that crystallization of garnet and clinopyroxene was coeval, followed by interstitial amphibole and plagioclase. Like in the previous sample and in most xenoliths from Mercaderes, 18XC5 displays evidence of pervasive reaction at all grain boundaries (Fig. 2c), probably related to entrainment in the lava. Quartz occurs as rare inclusions in garnet (Fig. 2d; see below).

Sample 18XC10 is a pyroxenite dominated by garnet, pyroxene and plagioclase, with minor, heterogeneously distributed hornblende (Supplementary Fig. S1c). The rock is fine-grained, with average grain-size of 1 mm and displays a mineralogical banding highlighted by 2- to 3-mm-thick monomineralic garnet layers (Supplementary Fig. S1c). The microstructure is granoblastic, and the monomineralic garnet layers show a polygonal texture derived from the impingement of growing grains. Unlike most of the crustal xenoliths from Mercaderes, sample 18XC10 displays a well-equilibrated texture (Fig. 2e), with neither sign of reaction between adjacent minerals nor of interaction with (or infiltration of) melt from the host lava. Igneous microstructures pointing to crystallization from melt are rarely observed and represented by plagioclase with crystal faces. The studied sections consist of two distinct zones (see Supplementary Fig. S2b) separated by a garnet rich layer: zone 1 consists of garnet, clinopyroxene and plagioclase in nearly equal amount with minor pargasitic amphibole; zone 2 mainly consists of garnet and clinopyroxene with interstitial plagioclase. Accessory rutile and apatite are equally distributed in both zones. The modal compositions for the two zones of sample 18XC10, determined through a SEM compositional map from an entire thin section (see Supplementary Fig. S2b), are as follows: 37.8 vol.% garnet, 33.4 vol.% clinopyroxene, 25.3 vol.% plagioclase, 3.2 vol.% amphibole and 0.3 vol.% rutile for zone1, and 58.1 vol.% garnet, 23.9 vol.% clinopyroxene, 15.8 vol.% plagioclase, 1.6 vol.% apatite and 0.6 vol.% rutile for zone 2. Quartz is present only as inclusions in garnet (Fig. 2f).

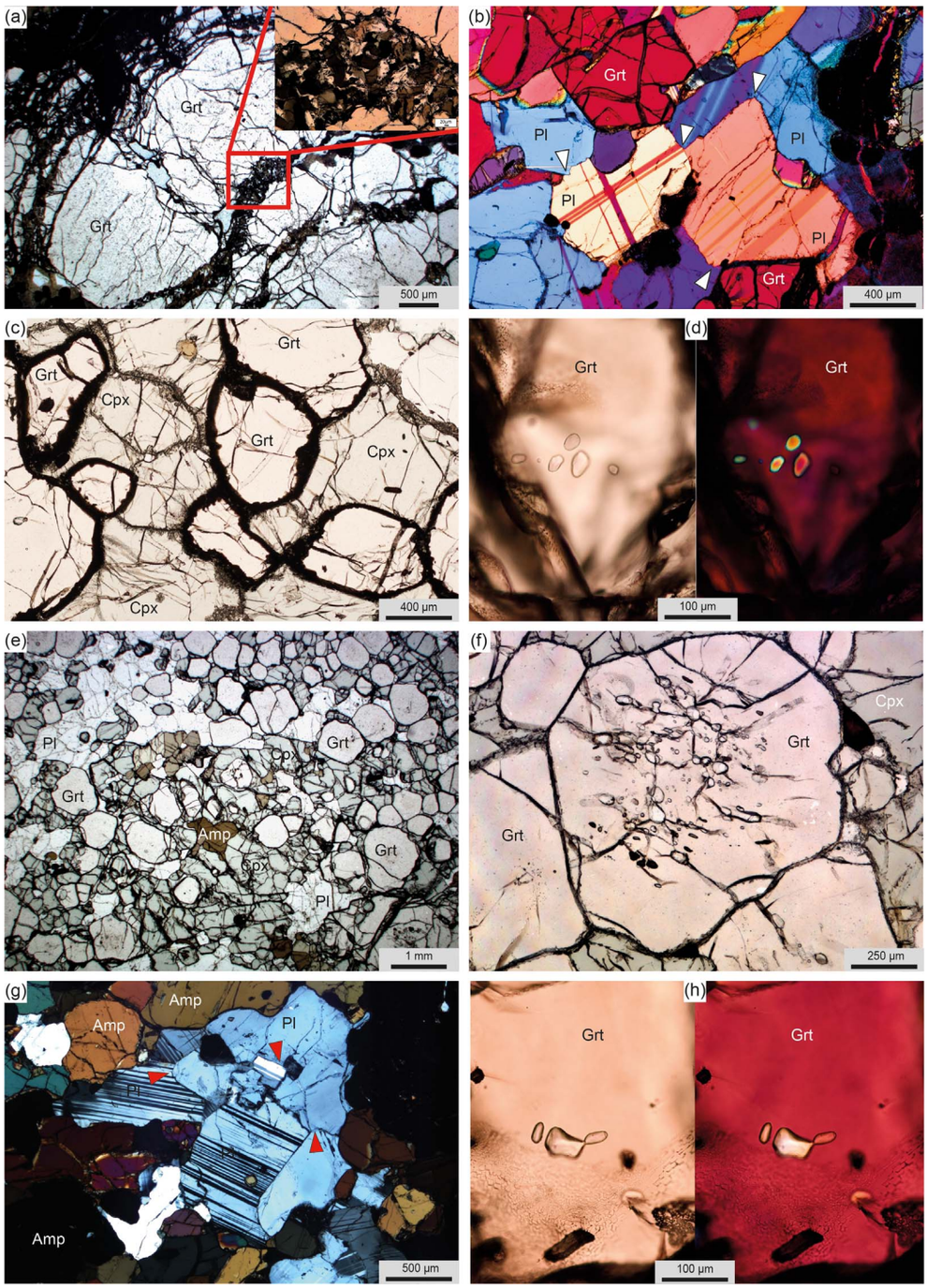

Fig. 2. Main petrographic features of the studied arclogite xenoliths. (a) Network of fractures filled with partly crystallized melt (detail in inset). Sample 18XC1, plane polarized light (PPL). (b) Plagioclase with planar crystal faces (arrows). Sample 18XC1, crossed polarizers (XPL) and lambda plate (λ). (c) Evidence of pervasive reaction along all grain boundaries. Sample 18XC5, PPL. (d) Quartz inclusions in garnet. Sample 18XC5, PPL (left) and XPL, λ (right). (e) Well equilibrated granoblastic texture of sample 18XC10. PPL. (f) Abundant primary quartz inclusions at the core of garnet. Sample 18XC10. PPL. (g) Plagioclase with euhedral crystal faces (arrows). Sample 18XC20, XPL. (h) Quartz inclusions in garnet, suggestive of *necking-down* processes. Sample 18XC20, PPL (left) and XPL, λ (right).

Sample 18XC20 is a banded xenolith with different Amp/Pl ratios. Garnet is abundant in both bands, whereas clinopyroxene is scarce. Although amphibole is the most abundant and coarser mineral, reaching up to 4 mm in size, it also occurs as inclusions in garnet and clinopyroxene. Garnet has a maximum diameter of 2 mm and may contain glass inclusions. Also plagioclase contains glass inclusions and, where abundant, displays euhedral shapes or interstitial positions (Fig. 2g), suggestive of crystallization from melt. This xenolith shows little evidence of reaction or resorption of crystals at grain boundaries, which are in most cases clean and well preserved. Quartz is present only as inclusions in garnet (Fig. 2h).

All samples contain rutile as accessory phase (Supplementary Fig. S1i), and all contain apatite.

Melt and mineral inclusions

Several types of inclusions occur in the main minerals of the studied xenoliths. We focus primarily on the inclusions hosted in garnet, as they are the object of further analyses and constrain the thermobarometric estimates and petrogenetic discussion made below. An extensive documentary of backscattered SEM images of MI is reported in the supplementary material (Supplementary Fig. S3).

Melt inclusions occur in garnet crystals from all samples. They are rare in 18XC1 and 18XC5, common in 18XC20, abundant in 18XC10. Their textural position, either isolated or scattered within the host, or more commonly arranged in the garnet cores (zonal arrangement after Roedder, 1984) indicates that the MI are primary in origin, i.e. they were trapped by the growing garnet (Fig. 3a, b). Occasional secondary MI locally form planar arrays. MI often display a negative crystal shape, more rarely rounded, and their size is generally <40 μm, with few larger MI reaching 100 μm (Fig. 3c-f). In samples 18XC10 and 18XC20, where MI in garnet are more abundant, they contain a single or multiple shrinkage bubbles (Fig. 3d, e; Roedder, 1984), and local evidence of necking down (Fig. 3d, f). The glass is optically fresh and colourless in 18XC10, whereas in 18XC20 it is more turbid and browner in colour (Fig. 3g). Under SEM imaging the MI in 18XC1, 18XC10 and 18XC20 often display the presence of nanolites made of a heavier phase (Fig. 3h and Supplementary Fig. S9).

MI occur in plagioclase from 18XC1 (Fig. 3i) and 18XC5, where they are, respectively, primary and secondary in origin. Very rarely, they are also observed in clinopyroxene from 18XC5 and 18XC10. In the latter sample the microstructures suggest a primary entrapment (Supplementary Fig. S1g). MI have also been observed in amphibole from 18XC1, where they display a tubular shape and appear secondary in origin (Supplementary Fig. S1h). Finally, SEM imaging allowed to detect MI also in oxide minerals such as rutile in 18XC1 (Fig. 3j). SEM also revealed the common occurrence of minute offshoots at MI boundaries, suggestive of overpressuring of the inclusions either by heating after entrapment or by decompression of the xenoliths during magma ascent.

MI may contain quartz (Fig. 3f) and rutile as trapped minerals, i.e. crystals, which were already present at the time of inclusion entrapment (Supplementary Fig. S1f, i).

Rutile occurs as solid inclusion in garnet in all samples, whereas zircon and quartz are observed in all except 18XC1. Rutile is observed both as small, crystallographically arranged needles suggesting exsolution from garnet, and as coarser crystals with variable aspect ratio (Fig. 3a, b; Supplementary Fig. S1i). In sample 18XC10, the rutile needles are located in a brownish intermediate annulus separating the inclusion-rich core from inclusion-free or inclusion-poor rims (Fig. 3b; Supplementary Fig. S1i). Zircon inclusions are particularly abundant, where they occur as crystals with 20 to 30 μm average size mostly located in the garnet cores.

Quartz inclusions in garnet are a key microstructure of most of the investigated crustal xenoliths at Mercaderes (Fig. 3a, b, f, k and Supplementary Fig. S1f), and their association with MI had already been highlighted by Weber *et al.* (2002). Quartz inclusions range from rare and scattered to very abundant, and display size from 10 to 150 μm. The shape of quartz inclusions ranges from spherical to slightly elongate and in places quartz inclusions display a strong shape preferred orientation (Fig. 2f and Fig. 3b). When observed in detail, quartz inclusions in garnet are faceted (Fig. 3k), as common in (U)HT rocks displaying shape maturation features (Cesare *et al.*, 2021).

Mineral chemistry

The complete dataset for the mineral chemistry of the analysed samples is reported in the Supplementary Table S5. Chemical analyses of garnets in sample 18XC1 (Fig. 4a) show that some crystals are slightly zoned, whereas some others display a marked zoning between core and rims. The slightly zoned minerals are characterized by subtle Fe-richer core compositions ($Alm_{36–40}Pyr_{29–34}Grs_{29–31}Sps_{0–1}$) compared to rims ($Alm_{34–38}Pyr_{30–31}Grs_{31–35}Sps_{0–1}$), whereas cores and rims in the zoned garnets are $Alm_{39–53}Pyr_{23–34}Grs_{22–31}Sps_{0–2}$ and $Alm_{32–39}Pyr_{29–31}Grs_{31–36}Sps_{0–1}$, respectively. Garnets in 18XC5 are Mg-richer (Fig. 4b) and do not show any zoning between cores ($Alm_{32–35}Pyr_{43–46}Grs_{21–23}Sps_{0–1}$) and rims ($Alm_{31–34}Pyr_{44–49}Grs_{19–21}Sps_{0–1}$). Garnets in 18XC10 are dominated by the almandine and pyrope components (Fig. 4c) and display a weak zoning in the grossular component between cores ($Alm_{38–42}Pyr_{38–43}Grs_{17–22}Sps_{0–1}$) and rims ($Alm_{38-43}Pyr_{40-44}Grs_{16-17}Sps_{0–1}$). In sample 18XC20, both homogeneous and zoned garnets have been observed. The zoned garnets (Fig. 4d) have cores slightly richer in Fe ($Alm_{47–49}Pyr_{27–29}Grs_{21–22}Sps_{2–3}$) compared with the rims ($Alm_{42–44}Pyr_{27–31}Grs_{26–27}Sps_{1–2}$), while the homogeneous garnets have cores with $Alm_{44–46}Pyr_{26–29}Grs_{25–26}Sps_{1–2}$ and rims with $Alm_{42–45}Pyr_{27–32}Grs_{24–28}Sps_{1–2}$.

Clinopyroxene crystals in sample 18XC1 (Fig. 5a) show a very weak zoning, with Al-richer (Al = 0.56–0.62 atoms per formula unit, a.p.f.u.) and lower X_{Mg} (X_{Mg} = 0.61–0.68, with X_{Mg} expressed hereafter as $[Mg/(Mg+Fe^{TOT})]$) rims compared with cores (Al = 0.52–0.57 a.p.f.u. and X_{Mg} = 0.66–0.69). On the other hand, the jadeite component (Jd) remains nearly constant between rims and cores (0.11–0.14 a.p.f.u.). From a stoichiometric point of view Cpx cores correspond to a composition equal to $Na_{0.11–0.14}Ca_{0.81–0.83}Al_{0.52–0.57}Fe_{0.23–0.26}Mg_{0.49–0.53}Si_{1.68–1.75}O_6$, whereas rims can be defined as $Na_{0.11–0.13}Ca_{0.74–0.82}Al_{0.56–0.62}Fe_{0.24–0.32}Mg_{0.47–0.51}Si_{1.67–1.73}O_6$. A single analysis of a Cpx inclusion in plagioclase shows the same composition as the cores of the Cpx in the matrix.

By contrast, Cpx crystals in 18XC5 do not display any zoning and are characterized by X_{Mg} and a Jd-component that range between 0.77–0.80 and 0.13–0.14 a.p.f.u., respectively. Their stoichiometric formula corresponds to $Na_{0.13–0.14}Ca_{0.77–0.79}Al_{0.33–0.37}Fe_{0.17–0.19}Mg_{0.62–0.67}Si_{1.85–1.89}O_6$, indicating that these pyroxenes are Al-poorer and Si- and Mg-richer than those observed in 18XC1.

A lack of zoning is also observed in the Cpx from sample 18XC10. In this sample, pyroxenes have a Jd content between 0.13 and 0.16 a.p.f.u. and a X_{Mg} ranging between 0.70 and 0.73. Additionally, Cpx display the lowest Al values (in a.p.f.u.) of all the analysed xenoliths, a feature that is emphasized by the general stoichiometric formula, $Na_{0.14–0.17}Ca_{0.72–0.76}Al_{0.27–0.30}Fe_{0.24–0.28}Mg_{0.64–0.68}Si_{1.86–1.91}O_6$.

For what concerns sample 18XC20, only a very weak zoning in Al can be observed in Cpx, with rims being enriched compared to cores (see Fig. 5b). Crystal cores and rims have a Jd-component between 0.17 and 0.20 a.p.f.u., while X_{Mg} is comprised between 0.63 and 0.67. The stoichiometric formula for cores corresponds to $Na_{0.17–0.19}Ca_{0.72–0.74}Al_{0.35–0.37}Fe_{0.29}Mg_{0.53–0.57}Si_{1.86–1.88}O_6$, whereas that of the rims is $Na_{0.17–0.20}Ca_{0.72–0.74}Al_{0.37–0.41}Fe_{0.29–0.31}Mg_{0.52–0.55}Si_{1.83–1.86}O_6$.

Amphibole crystals from sample 18XC1 are not zoned, with Si = 5.71–5.99 a.p.f.u., Ca = 1.70–1.79 a.p.f.u., Na = 0.62–0.77 a.p.f.u. and X_{Mg} = 0.62–0.65 (Supplementary Table S5). In general,

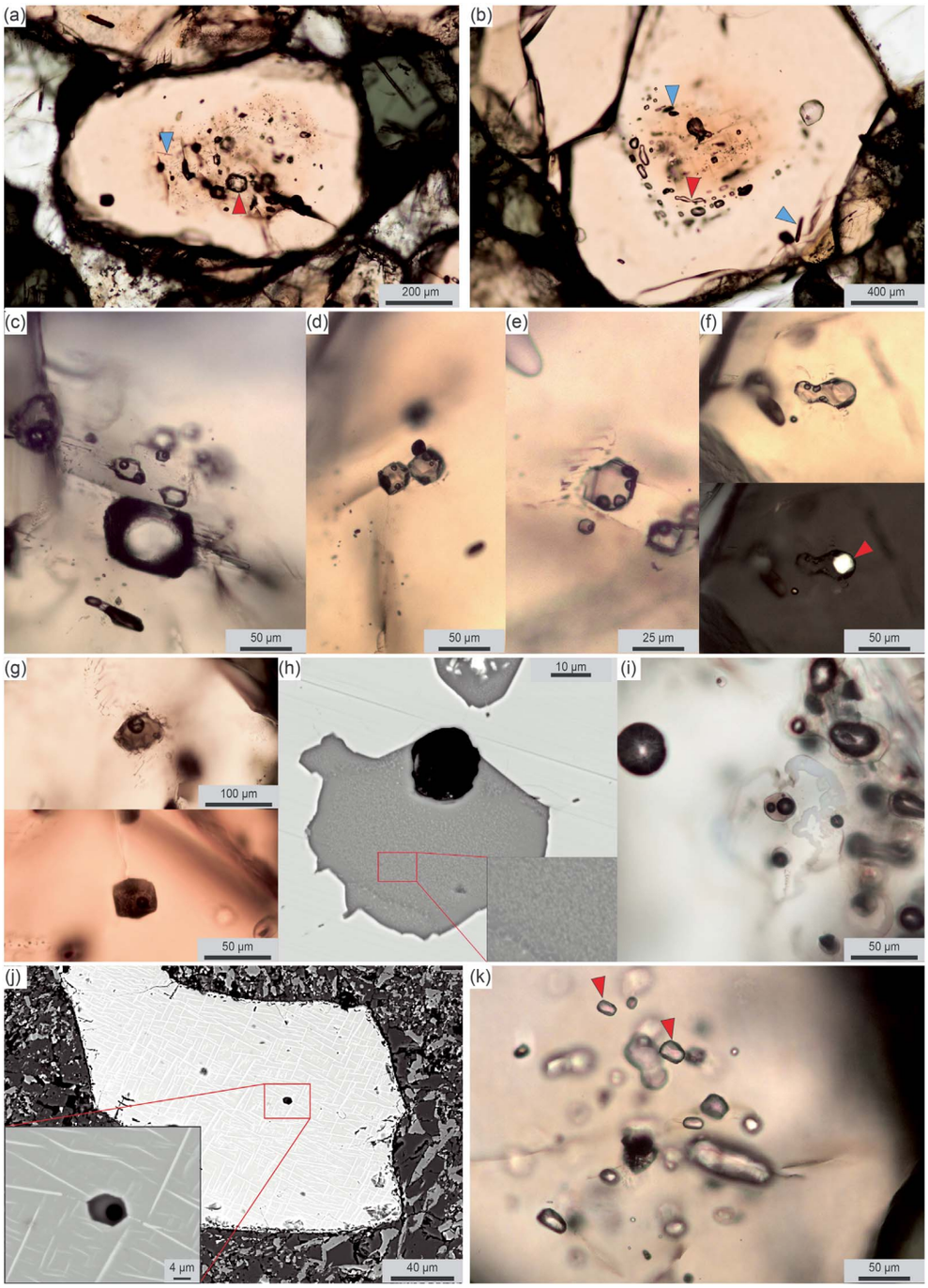

Fig. 3. Main microstructures of inclusions in rock-forming minerals of the studied arclogite xenoliths. See text for further details. Inclusions are hosted in garnet except (i) and (j), hosted in plagioclase and rutile, respectively. All micrographs taken in PPL mode, except (f, bottom) taken under XPL, and (h) and (j), taken under BSE imaging. (a) 'Zonal arrangement' of primary inclusions of glass (red arrow), rutile (blue arrow) and quartz. (b) 'Zonal arrangement' of primary inclusions of quartz, rutile (blue arrows) and glass. The red arrow points at an elongate quartz inclusion suggestive of *necking-down* processes (c-e) Examples of MI with negative crystal shape and one or more shrinkage bubbles. (f) Elongate MI with evidence of *necking-down*, multiple shrinkage bubbles, and one trapped crystal of quartz (red arrow on bottom view). (g) Examples of dark brown glass in MI from sample 18XC20. (h) Nanolites in the glass of a MI in sample 18XC1. Close-up in inset. (i) Primary MI in plagioclase from sample 18XC1. (j) Primary MI in rutile from sample 18XC1. Detail in inset, also showing exsolution textures. (k) Faceted inclusions of quartz (red arrows) trapped in garnet.

the amphiboles in 18XC1 can be classified as ferroan-pargasite. Rim-core analyses of a single amphibole grain in 18XC5 show that the crystal is pargasitic in composition and has rims slightly depleted in Mg (3.04–3.08 a.p.f.u.) compared to the core (3.12–3.14 a.p.f.u.). For what concerns the other elements, Si varies between 6.12 and 6.15 a.p.f.u., Ca and Na between 1.60–1.64 and 0.77–0.81 a.p.f.u., respectively, while X_{Mg} is comprised between 0.75 and 0.76 for both core and rim. In sample 18XC10 amphiboles

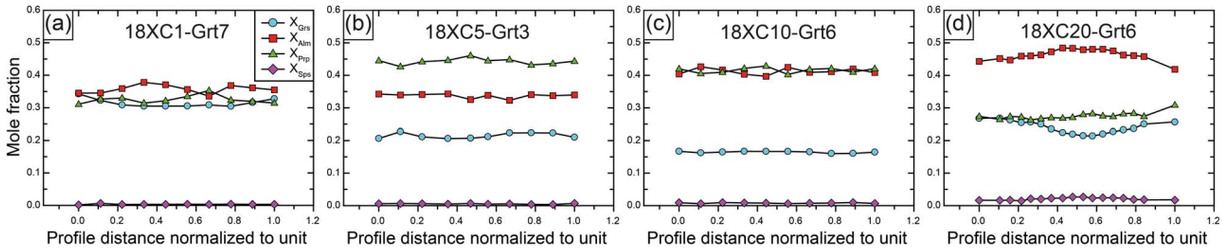

Fig. 4. Representative garnet profiles (rim to rim) for the Mercaderes xenoliths. $X_{Grs} = Ca/(Ca + Fe^{2+} + Mg + Mn)$, $X_{Alm} = Fe^{2+}/(Ca + Fe^{2+} + Mg + Mn)$, $X_{Prp} = Mg/(Ca + Fe^{2+} + Mg + Mn)$ and $X_{Sps} = Mn/(Ca + Fe^{2+} + Mg + Mn)$. Uncertainties on analyses are smaller than the symbol size.

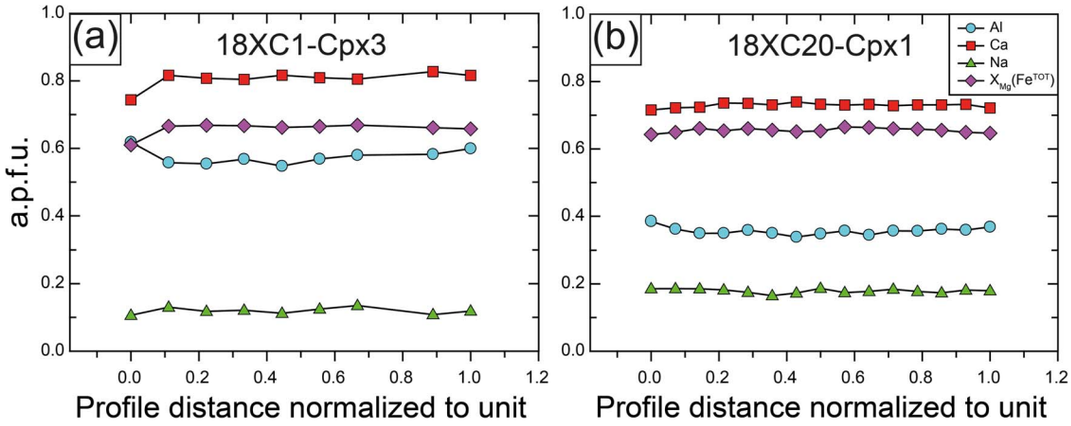

Fig. 5. Representative clinopyroxene profiles (rim to rim) for the Mercaderes xenoliths. Cations given in atoms per formula units (a.p.f.u.). $X_{Mg} = Mg/(Mg + Fe^{TOT})$ and, therefore, dimensionless. Uncertainties on analyses are smaller than the symbol size.

are also pargasitic and do not display zoning, with Si = 6.10–6.16 a.p.f.u., Ca = 1.51–1.55 a.p.f.u., Na = 0.82–0.94 a.p.f.u. and X_{Mg} = 0.67–0.70. In sample 18XC20 amphiboles from the matrix, as well as those included in garnet and Cpx, were measured. The amphiboles from the matrix have composition ranging from ferroan-pargasite to pargasite, with Si = 5.83–6.14 a.p.f.u., Ca = 1.51–1.63 a.p.f.u., Na = 0.79–0.95 a.p.f.u. and X_{Mg} = 0.56–0.59 (Fig. 6a). On the other hand, the amphibole inclusions measured in different garnet grains have a chemical composition that ranges from cummingtonite (Si = 6.19–6.39 a.p.f.u., Ca = 1.19–1.22 a.p.f.u., Na = 0.44–0.62 a.p.f.u., X_{Mg} = 0.58) to ferroan-pargasite (Si = 5.87–6.01 a.p.f.u., Ca = 1.65–1.66 a.p.f.u., Na = 0.67–0.72 a.p.f.u., X_{Mg} = 0.51–0.60). By contrast, the amphibole inclusions found in different clinopyroxene crystals are more homogeneous, showing a ferroan-pargasitic composition, with Si = 5.90–5.98 a.p.f.u., Ca = 1.60–1.63 a.p.f.u., Na = 0.93–0.95 a.p.f.u. and X_{Mg} = 0.56–0.58.

The plagioclase crystals observed in 18XC1 are not zoned and have a X_{An} [$X_{An} = Ca/(Ca + Na + K)$] that ranges between 0.48 and 0.55, corresponding to andesine-labradorite. By contrast, a plagioclase vein within garnet displays a nearly pure anorthitic composition (X_{An} = 0.92–0.98).

Plagioclase from sample 18XC10 is homogeneous and has a distinctive oligoclasic composition (X_{An} = 0.25–0.27). On the other hand, some plagioclases in 18XC20 show a very weak zoning (see Fig. 6b), with Ca-richer rims (X_{An} = 0.29–0.30) compared to cores (X_{An} = 0.27–0.28). A plagioclase pocket interstitial between two garnets shows different intergrowths with compositions that vary between X_{An} = 0.29–0.30 and X_{An} = 0.51–0.55. Plagioclase inclusions in garnets display a large variety of compositions (in different garnet crystals but also within the same grain), with X_{An} between 0.28 and 0.61 (oligoclase to andesine).

Scapolite crystals measured in 18XC1 (Fig. 6c) and 18XC5 are characterized by high concentrations in sulphur, with SO_3 that ranges between 3.1 and 5.4 wt.% and, therefore, can be defined as silvialite. All the measured scapolites are not zoned, showing a meionite component [Me% = $(Ca + Mg + Fe^{2+} + Mn + Ti)/(Na + K + Ca + Mg + Fe^{2+} + Mn + Ti) \cdot 100$] between 69 and 73.

Major and trace element compositions of melts

Glass was analysed mostly not only in melt inclusions but also in veinlets that infiltrated garnets and in interstitial films, the latter probably containing the host lava which entered the xenoliths (see Supplementary Table S6). Overall, the analysed melts cover a SiO_2 range from 57.5 wt.% to 75.3 wt.%, forming distinct clusters for each type of xenolith in the TAS diagram (Le Bas *et al.*, 1986; Fig. 7a). Melts with the lowest silica contents are observed in sample 18XC1 (57.5–63.5 wt.%), which are followed, with increasing SiO_2, by analyses from samples 18XC20 (61.3–72.0 wt.%), 18XC5 (70.7–71.4 wt.%) and sample 18XC10 (69.1–75.2 wt.%). The average SiO_2 contents (on anhydrous basis and normalized to 100%) for the analysed melt inclusions are as follows: 60.9 ± 1.4 wt.% for 18XC1, 65.3 ± 1.1 wt.% for 18XC20, 71.2 ± 0.3 wt.% for 18XC5 and 72.4 ± 0.6 wt.% for 18XC10 (all errors expressed as 2 standard error of the mean, 2 s.e.m., see also Table 1). According to the TAS classification, melts in sample 18XC1 are dominantly andesitic in composition, those from sample 18XC20 are trachytic to dacitic, while melts from 18XC5 and 18XC10 are mainly rhyolitic (Fig. 7a). When plotted in the An–Or–Ab diagram (O'Connor, 1965; Supplementary Fig. S4) the analysed melt inclusions for 18XC1 lie prevalently in the granodioritic field, those for 18XC5 and 18XC10 are dominantly trondhjemitic, while MI in 18XC20 range from tonalite to trondhjemite in composition. The interstitial melts in 18XC10 and 18XC20 are tonalitic and granitic,

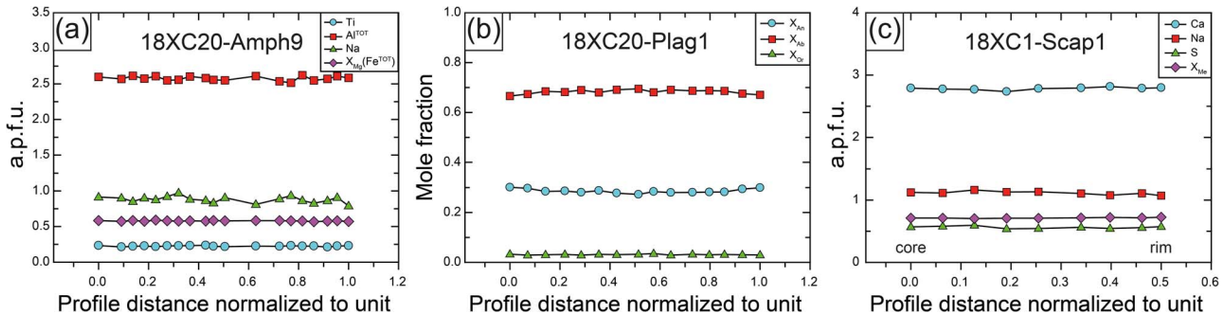

Fig. 6. Representative profiles for amphibole (a), plagioclase (b) and scapolite (c) for the Mercaderes xenoliths. Cations given in atoms per formula units (a.p.f.u.). Ratios are defined as following: $X_{Mg} = Mg/(Mg + Fe^{TOT})$, $X_{An} = Ca/(Ca + Na + K)$, $X_{Ab} = Na/(Ca + Na + K)$, $X_{Or} = K/(Ca + Na + K)$ and $X_{Me} = (Ca + Mg + Fe^{2+} + Mn + Ti)/(Na + K + Ca + Mg + Fe^{2+} + Mn + Ti)$ are all dimensionless. The profiles for amphibole and plagioclase are rim to rim, whereas the profile for scapolite is core to rim. Uncertainties on analyses are smaller than the symbol size.

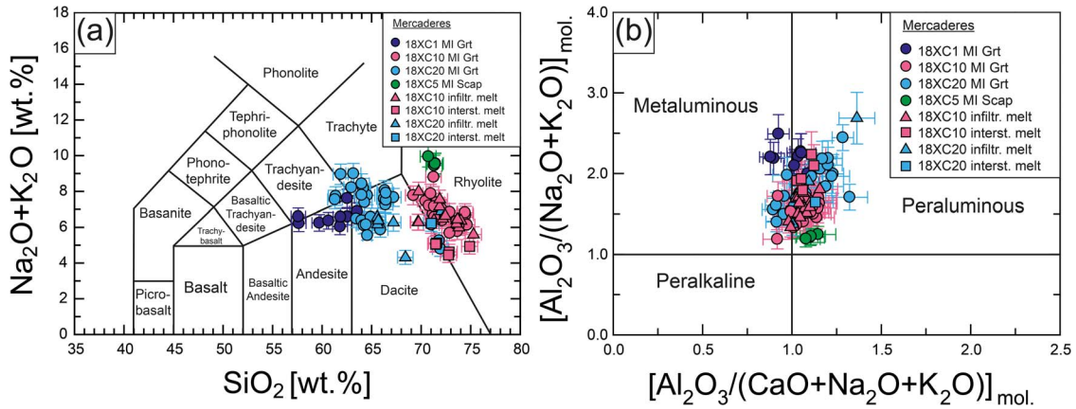

Fig. 7. Chemical classification of the glasses analysed in the Mercaderes xenoliths (normalized to 100% on anhydrous basis). (a) TAS diagram. (b) Aluminium saturation index versus alkalinity index. Errors on analyses are reported as 2 s.

respectively, whereas the infiltrated melts in the same samples are mainly scattered across the tonalitic and trondhjemitic fields (Supplementary Fig. S4). Moreover, most of the melts observed in the xenoliths display a peraluminous character (Fig. 7b). In Harker diagrams (Fig. 8a–k) sample 18XC1 is characterized by a negative correlation with SiO_2 for TiO_2 (although this correlation becomes positive for $TiO_2 < 0.3$ wt.%), FeO and MgO, whereas Al_2O_3, Na_2O, K_2O and P_2O_5 show a nearly constant correlation with increasing silica. Moreover, some of the MI measured in sample 18XC1 have the highest concentrations in CaO, FeO and MgO. MI in sample 18XC20 are negatively correlated with SiO_2 for Al_2O_3, whereas for CaO and Na_2O a negative trend is present, but less pronounced. The infiltrated melt measured in 18XC20 shows a negative correlation with increasing silica for Al_2O_3, CaO, MgO and slightly also for P_2O_5, whereas for TiO_2, Na_2O and K_2O, the trend remains constant. MI analysed for sample 18XC10 show a strong negative correlation with SiO_2 for Al_2O_3, while for FeO, MgO and Na_2O, the negative trend is less defined. All other elements are highly scattered, and no correlation with silica can be observed. The infiltrated melt measured in 18XC10 shows a clear negative correlation for Al_2O_3, whereas the other oxides display a large scattering. On the other hand, the interstitial melt in 18XC10 is characterized by a negative trend for TiO_2, Al_2O_3, CaO, P_2O_5, and in a lesser extent also for FeO and MgO vs. SiO_2, whereas for Na_2O and K_2O, the trend is almost constant. Remarkable is the high variability in P_2O_5 displayed by the interstitial melt, which was measured in two different locations of a mm-sized melt pocket, with analyses between 0.34 and 0.64 wt.% P_2O_5 that belong to the same location.

In the absence of a direct quantification of H_2O in the glasses, the EPMA analytical totals of MI suggest that the melts within MI may have a moderate H_2O content of about 2.3 ± 0.8 wt.% (2 s.e.m.) in sample 18XC1, 1.0 ± 0.4 wt.% (2 s.e.m.) in sample 18XC10 and 2.7 ± 0.6 wt.% (2 s.e.m.) in sample 18XC20. The glass in the MI in scapolite from sample 18XC5 and the interstitial melt in sample 18XC10 may be slightly more hydrous, with up to 4.5 wt.% H_2O.

Trace elements vs. SiO_2 show a negative trend for Rb and U + Th in MI from sample 18XC20, which display the highest concentrations for these elements, and a weak positive correlation for Zr in both 18XC20 and 18XC10, with the latter sample showing the highest concentrations (up to 152 μg/g). Another distinctive feature observed in 18XC10 is that the interstitial melt has lower U + Th concentrations compared with the MI. Comparable low concentrations in U + Th can be noticed also for a MI analysed in 18XC1, which by contrast has Rb and Zr concentrations, like 18XC20.

Trace elements normalized to the primitive mantle (McDonough & Sun, 1995) display very similar patterns, with a strong enrichment in large ion lithophile elements (LILE), a marked Nb–Ta anomaly, a strong positive anomaly for Pb and a weak to strong positive anomaly for Sr (Fig. 9a–c). Analyses of the interstitial melt measured in sample 18XC10 show lower U and K concentrations, a weaker Nb–Ta anomaly and a positive P anomaly compared to the other melts.

Table 1: Average chemical compositions of the analysed glasses. Errors are expressed as two standard error of the mean (2 s.e.m.)

	Melt inclusions						Infiltrated melts						Interstitial melt	
	18XC1 (wt.%)	2 s.e.m.	18XC5 (wt.%)	2 s.e.m.	18XC10 (wt.%)	2 s.e.m.	18XC20 (wt.%)	2 s.e.m.	18XC20 (wt.%)	2 s.e.m.	18XC10 (wt.%)	2 s.e.m.	18XC10 (wt.%)	2 s.e.m.
SiO_2	60.87	1.43	71.21	0.33	72.39	0.62	65.34	1.09	67.41	2.07	72.33	0.95	72.49	1.09
TiO_2	0.38	0.13	0.46	0.04	0.36	0.03	0.25	0.07	0.20	0.03	0.40	0.04	0.33	0.11
Al_2O_3	20.09	0.33	17.33	0.14	14.99	0.41	18.40	0.75	16.27	0.98	14.98	0.60	14.74	0.50
FeO	4.66	1.39	0.36	0.09	2.39	0.31	3.86	0.45	5.25	0.70	2.32	0.51	2.99	0.20
MnO	0.18	0.06	-	-	0.10	0.05	0.18	0.03	0.15	0.06	0.09	0.04	0.13	0.04
MgO	1.18	0.46	0.21	-	0.73	0.12	1.11	0.15	1.31	0.18	0.77	0.20	0.63	0.06
CaO	6.01	0.83	0.78	0.07	2.29	0.24	3.73	0.33	3.30	0.52	2.56	0.26	3.49	0.27
Na_2O	3.84	0.31	6.80	0.27	4.64	0.36	5.03	0.42	4.33	0.77	4.36	0.35	3.88	0.21
K_2O	2.73	0.12	2.83	0.18	2.14	0.20	2.09	0.14	1.77	0.07	2.20	0.21	1.00	0.04
P_2O_5	0.12	0.02	0.18	0.04	0.12	0.01	0.14	0.02	0.10	0.02	0.15	0.02	0.35	0.15
Total anhydrous	100.00	-	100.00	-	100.00	-	100.00	-	100.00	-	100.00	-	100.00	-
Total EPMA	97.68	0.80	95.54	0.71	99.00	0.40	97.32	0.64	98.56	0.50	99.24	0.16	96.45	1.21
$Na_2O + K_2O$	6.57	0.31	9.63	0.23	6.78	0.30	7.12	0.45	6.10	0.74	6.55	0.33	4.88	0.22
$[Al_2O_3/(Na_2O + K_2O)]_{molar}$	2.18	0.11	1.22	0.02	1.52	0.05	1.78	0.10	1.86	0.36	1.58	0.07	1.98	0.13
$[Al_2O_3/(CaO + Na_2O + K_2O)]_{molar}$	1.00	0.05	1.11	0.03	1.07	0.03	1.08	0.05	1.09	0.11	1.06	0.02	1.07	0.03
$[K_2O/Na_2O + K_2O]_{molar}$ x 100	32.08	2.10	21.52	1.57	23.64	2.38	21.99	1.77	21.92	4.62	25.15	2.70	14.55	0.67
$Na_2O + K_2O$-CaO	0.56	1.03	8.85	0.18	4.49	0.42	3.39	0.48	2.80	0.98	3.99	0.44	1.39	0.37

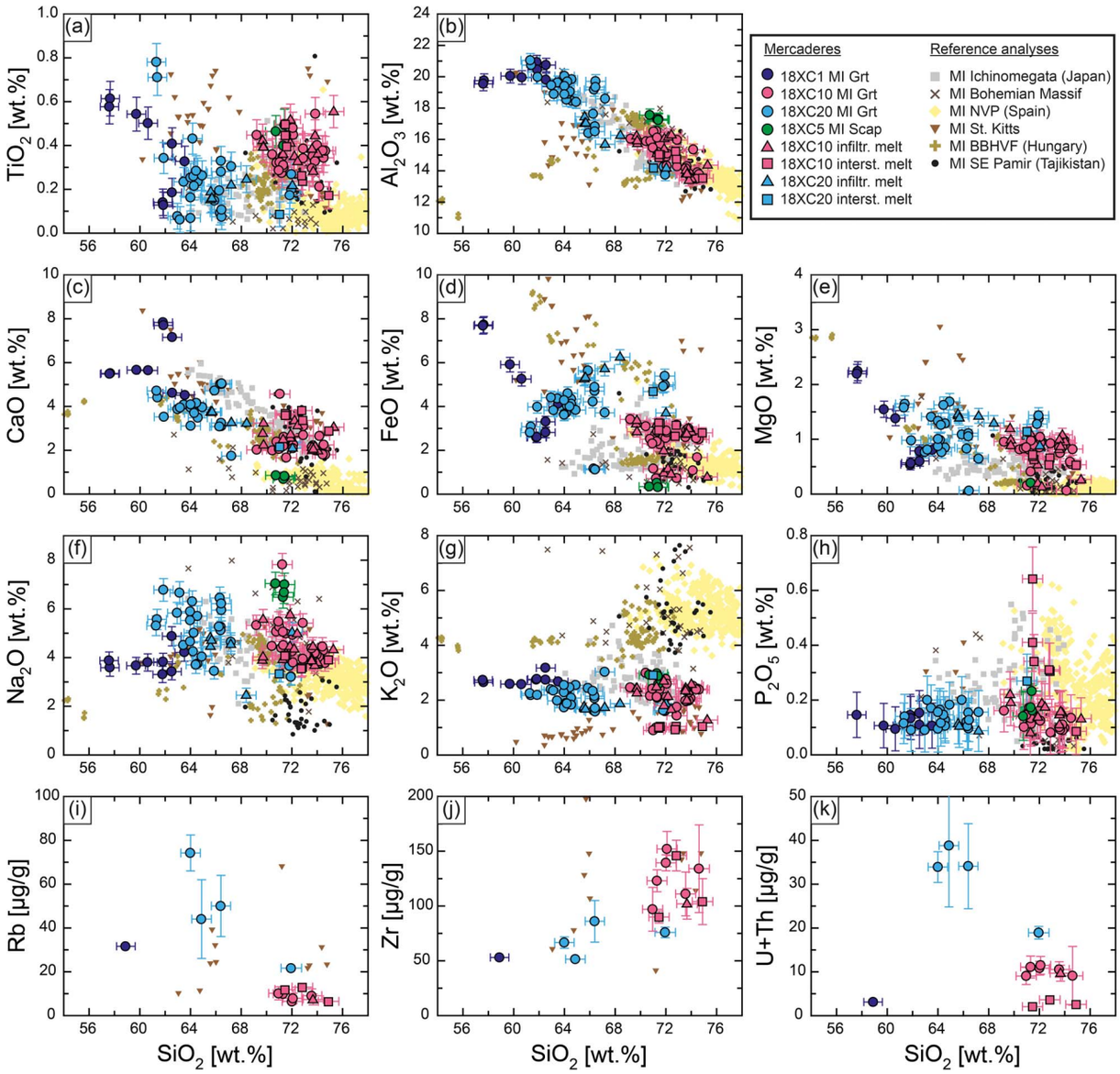

Fig. 8. (a-k) Harker diagrams for the analysed glasses. Reference analyses for the Ichinomegata arc are from Yanagida *et al.* (2018); for the Bohemian Massif from Borghini *et al.* (2018), Borghini (2020) and Ferrero *et al.* (2019); for the Neogene Volcanic Province (NVP) from Acosta-Vigil *et al.* (2007), Bartoli *et al.* (2016), Cesare *et al.* (2003) and Ferrero *et al.* (2011); for the St. Kitts arc from Melekhova *et al.* (2017); for the Bakony–Balaton Highland Volcanic Field (BBHVF) from Németh *et al.* (2021) and from south-eastern Pamir (Chupin *et al.*, 2006). All analyses normalized to 100% on anhydrous basis. Errors on analyses are reported as 2 s.

Geothermobarometry

Pressure and temperature conditions were determined by conventional geothermobarometry for all the investigated samples alongside with a detailed investigation by phase equilibria modelling, intracrystalline geothermometry (Fe–Mg order–disorder on clinopyroxene) and elastic geothermobarometry for sample 18XC10 (Fig. 10a–b), which displays a particularly well-equilibrated mineral assemblage.

Conventional geothermobarometry was carried out using the thermometers of Nakamura (2009) and Sudholz *et al.* (2022), which are based on Fe–Mg exchange between garnet and clinopyroxene, and the barometer of Beyer *et al.* (2015). Uncertainty on temperature was calculated by error propagation using the *Metas.UncLib* Python script (Zeier *et al.*, 2012), while for pressure, we assumed the maximum error as reported in Beyer *et al.* (2015). In general, the intersections of the geothermometers with the geobarometer give similar results (see Table 2 and Supplementary Fig. S5). The highest temperatures and pressures are observed for the rim analysis of a Grt–Cpx pair from sample 18XC1, with values up to 1480°C and 3.0 GPa, while sample 18XC5 shows temperatures between 960°C and 1030°C and pressures between 1.3 and 1.6 GPa. A similar range, within error, is also observed for 18XC10, whereas 18XC20 displays slightly higher values, with temperature and pressure that range from 1100°C to 1130°C and 1.3 and 1.9 GPa, respectively.

For what concerns intracrystalline geothermometry, on the basis of the pyroxene chemical analyses, the calibration reported in equation 4 by Brizi *et al.* (2000) has been adopted to determine

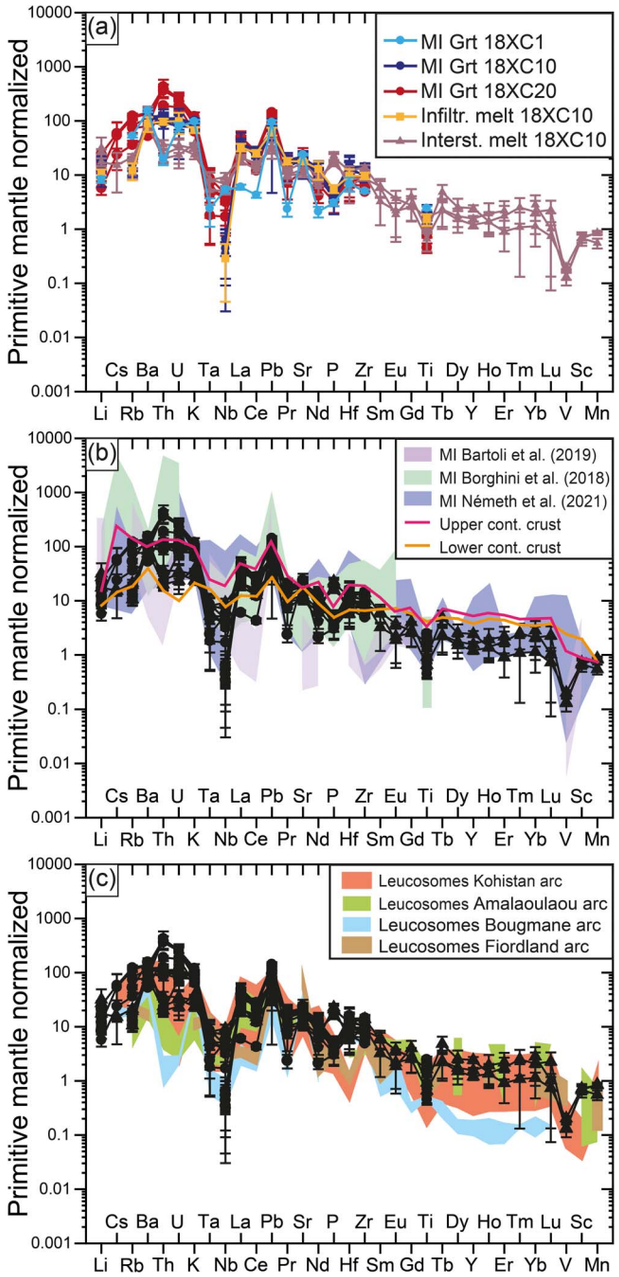

Fig. 9. Normalized trace element patterns. (a) Melt inclusions (MI), infiltrated and interstitial melt from the Mercaderes xenoliths. (b) Comparison with MI from Himalaya (Bartoli *et al.*, 2019), Bohemian Massif (Borghini *et al.*, 2018; Ferrero *et al.*, 2019) and the Bakony–Balaton Highland Volcanic Field (Németh *et al.*, 2021). (c) Comparison with anatectic leucosomes from the Kohistan arc (Garrido *et al.*, 2006), the Amalaoulaou arc (Berger *et al.*, 2011), the Bougmane arc (Triantafyllou *et al.*, 2018) and from the Fiordland arc (Daczko *et al.*, 2001). Error bars are expressed as 2 standard error of the mean.

the closure temperature on seven pyroxene crystals of sample 18XC10. The resulting temperatures range from 1050°C to 1140°C, with a calculated average at 1090 ± 30°C (2 s.e.m.) (Fig. 10b and Supplementary Table S4).

Phase equilibria modelling for sample 18XC10 was performed starting from a bulk rock composition (see caption to Fig. 10) determined combining the mineral proportions estimated from an entire SEM compositional map (see Supplementary Fig. S2b) and the mineral chemistry acquired by EPMA. Although the thin section shows two distinct zones (see above), the mode of the entire thin section (54.3 vol.% garnet, 25.0 vol.% clinopyroxene, 18.0 vol.% plagioclase, 2.0 vol.% amphibole, 0.5 vol.% rutile and 0.2 vol.% apatite) was used, since the chemical compositions of the minerals are the same in both zones. Calculations indicates that the peak mineral assemblage observed in sample 18XC10 (Grt–Cpx–Pl–Amp–Rt melt) is predicted to be stable in a P–T field located at 1.5 to 1.8 GPa and 850°C to 1080°C (Fig. 10a). The low-T boundary of such field corresponds to the calculated solidus, and quartz is predicted to be stable just below the solidus. Amphibole disappears at about 1050°C in this pressure range. Calculated modal proportions of each mineral phase (isomodes) reproduce the amounts of minerals present in 18XC10 (see Supplementary Fig. S6). As an example, at 1000°C and 1.7 GPa, the model predicts the following mineral modes: 57.2 vol.% garnet, 25.5 vol.% clinopyroxene, 15.3 vol.% plagioclase, 0.9 vol.% amphibole and 0.4 vol.% rutile, in agreement with the observed mineral mode. Conversely, when compositional isopleths are plotted on the phase diagram (Supplementary Fig. S6), the predicted compositions of phases in the Grt–Cpx–Pl–Amp–Rt melt field do not completely match the measured ones. In particular, modelled garnet composition is more calcic, clinopyroxene is more magnesian, and plagioclase is more albitic. On the other hand, the model shows a better fit for the almandine and pyrope components of garnet, as well as for the jadeite content in clinopyroxene.

Each sample displays a characteristic, relatively narrow, range of H_2O contents in the glasses of MI. Along with the lack of decrepitation textures, such sample-specific melt H_2O contents point against H_2O loss or gain from glass inclusions. Assuming that they represent the original values, also, the H_2O contents of MI inferred from the EPMA total closure can be used to constrain the P–T conditions of their entrapment. In particular, at a given pressure, they can provide the minimum temperature at which that melt may occur. Extrapolation to higher pressures of the experiments on the haplogranite system (Holtz *et al.*, 2001; Makhluf *et al.*, 2017) would suggest temperatures >1100°C for sample 18XC10, >1050°C for samples 18XC1 and 18XC20, and ~950°C for 18XC5, at a reference pressure of 1.5 GPa. These temperatures vary as a function of pressure with a dependence of about 200°C/GPa in the P–T region of interest (Makhluf *et al.*, 2017).

Results from Raman measurements on zircon and quartz inclusions from sample 18XC10 are shown in Fig. 10b and Fig. 11 and reported in the Supplementary Table S3.

The P_{inc} of quartz inclusions is the same in a 2σ uncertainty for inclusions both within the same garnet and amongst different garnets. Zircon inclusions were found only within one garnet but also show similar inclusion pressure within their uncertainties. Therefore, we averaged the P_{inc} of the same inclusions from the same growth zone (least-squares weighted average, using the uncertainty on P_{inc} as weighing factor) to calculate one representative entrapment isomeke for quartz (average $P_{inc} = 0.02 \pm 0.05$ GPa, 2 s.e.m.) and one for zircon (average $P_{inc} = 1.09 \pm 0.03$ GPa, 2 s.e.m.; Fig. 11). The average P_{inc} for zircons and quartz suggest a P–T range of 1150 ± 30°C (2 s.e.m.) and 1.9 ± 0.2 GPa (2 s.e.m.) (Fig. 10b). Such P–T values for 18XC10 are consistent with those obtained from the other applied methods (i.e. conventional geothermobarometry, phase equilibria and intracrystalline geothermometry) and also with the peak metamorphic conditions suggested by Bloch *et al.* (2017) for the Mercaderes arclogites.

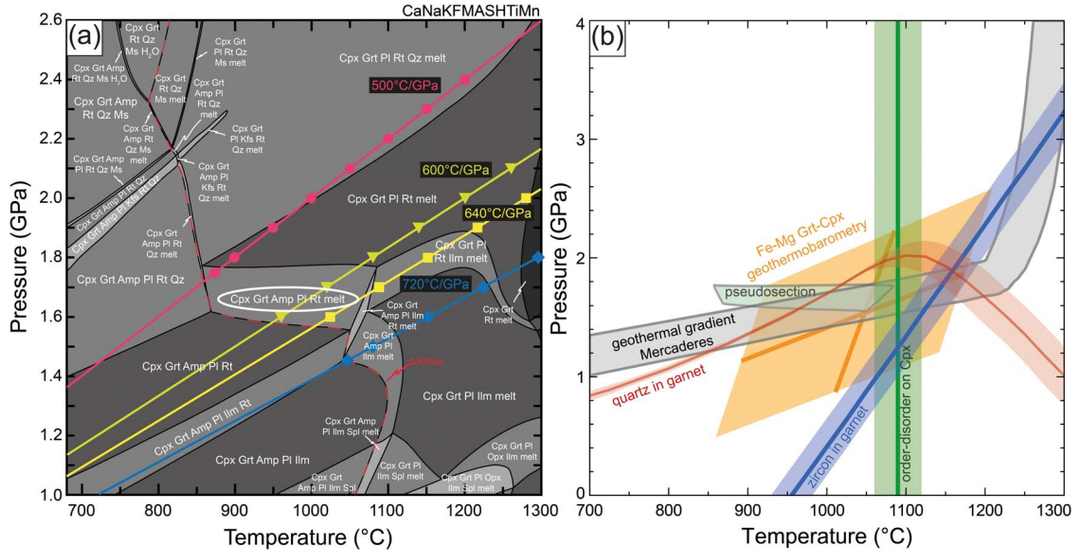

Fig. 10. Geothemobarometry for sample 18XC10. (a) Phase equilibria modelling with Perple_X using the following bulk rock composition: SiO_2 = 46.61 wt.%, Al_2O_3 = 17.61 wt.%, MgO = 10.19 wt.%, FeO = 13.11 wt.%, MnO = 0.27 wt.%, CaO = 9.79 wt.%, Na_2O = 1.79 wt.%, K_2O = 0.07 wt.%, TiO_2 = 0.53 wt.% and H_2O = 0.04 wt.%. The bulk rock composition was determined combining the mineral proportions estimated from a SEM compositional map and the mineral chemistry acquired by EPMA. The ellipse highlights the stability field of the xenolith. Different geothermal gradients are also displayed. Points on the geothermal gradients represent P–T conditions above the solidus at which the density of the system (residue + melt) was investigated with Perple_X. (b) Summary of all the geothermobarometric methods applied on sample 18XC10. The geothermal gradient calculated by Bloch *et al.* (2017) is also shown.

Table 2: Conventional geothermobarometry. Errors on pressure and temperature are expressed as two standard error of the mean (2 s.e.m.)

	Nakamura (2009)		Beyer *et al.* (2015)		Sudholz *et al.* (2022)		Beyer *et al.* (2015)	
	T (°C)	2 s.e.m.	P (GPa)	2 s.e.m.	T (°C)	2 s.e.m.	P (GPa)	2 s.e.m.
18XC1								
18XC1 Grt-Cpx rim 1	1477	60	3.00	0.4	1399	26	2.77	0.4
18XC1 Grt-Cpx core 1	1264	127	2.14	0.4	1210	107	1.99	0.4
18XC5								
18XC5 Grt-Cpx rim 1	992	27	1.30	0.4	1008	24	1.34	0.4
18XC5 Grt-Cpx core 1	966	29	1.40	0.4	977	24	1.43	0.4
18XC5 Grt-Cpx rim 2	1021	63	1.48	0.4	1033	56	1.51	0.4
18XC5 Grt-Cpx core 2	960	39	1.54	0.4	972	31	1.58	0.4
18XC5 Grt-Cpx rim 3	1028	44	1.53	0.4	1034	40	1.54	0.4
18XC5 Grt-Cpx core 3	963	50	1.38	0.4	978	45	1.42	0.4
18XC10								
18XC10 Grt-Cpx rim 1	1021	85	1.30	0.4	1079	80	1.44	0.4
18XC10 Grt-Cpx core 1	1034	114	1.68	0.4	1083	109	1.82	0.4
18XC20								
18XC20 Grt-Cpx rim 1	1119	54	1.82	0.4	1129	51	1.85	0.4
18XC20 Grt-Cpx rim 2	1105	76	1.75	0.4	1120	74	1.79	0.4
18XC20 Grt-Cpx rim 3	1111	94	1.86	0.4	1126	91	1.91	0.4

DISCUSSION

Petrographic constraints from microstructures

The present research builds extensively on information provided by inclusions in the main rock-forming minerals of the xenoliths, in particular by inclusions in garnet.

MI in crustal xenoliths are more common in volcanic rocks from extensional settings (e.g. the Pannonian Basin, Németh *et al.*, 2021; the Neogene Volcanic Province of SE Spain, Acosta-Vigil *et al.*, 2007) than in continental arcs (e.g. Pamir, Chupin *et al.*, 2006). At Mercaderes, the occurrence of melt and quartz inclusions in

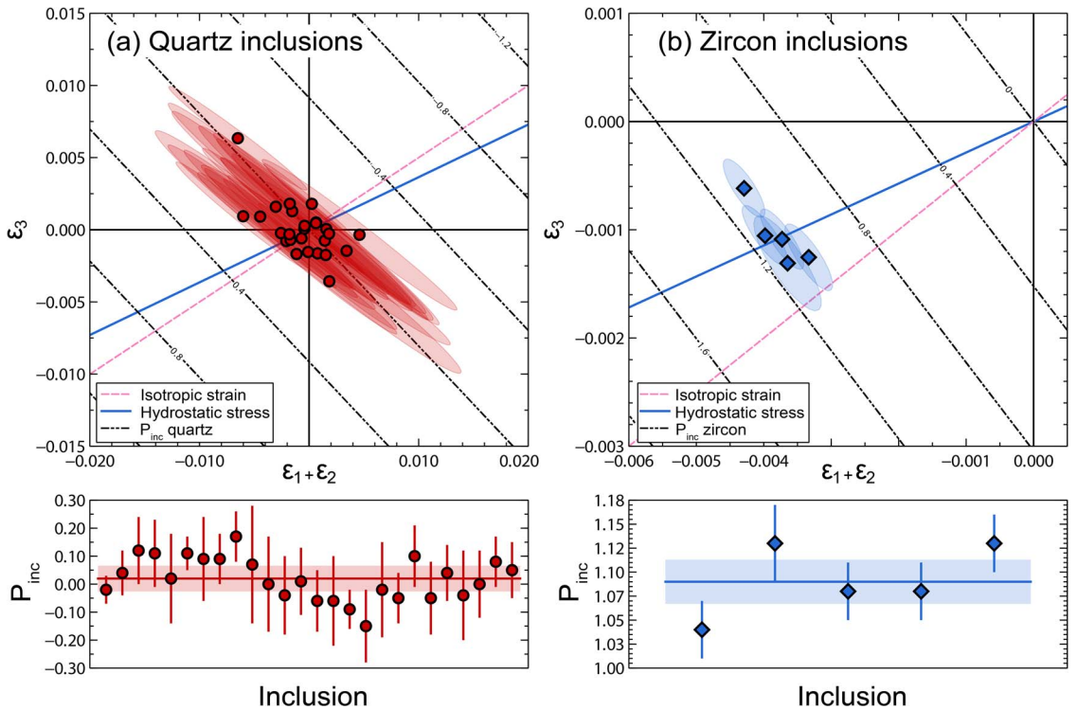

Fig. 11. Strains and inclusion pressure of quartz and zircon inclusions in garnet. (a) Quartz. (b) Zircon. The hydrostatic stress lines of quartz and zircon (solid blue lines) and those of equal inclusion pressure (dash-dot lines in black) were produced by converting the strain into stress with the available elastic tensor for quartz (Wang *et al.*, 2015) and zircon (Özkan *et al.*, 1974), disregarding stiffening or softening effects with pressure. The uncertainty on P_{inc} was obtained by propagating the uncertainty on strain (the variance–covariance matrix) through the procedure described in Mazzucchelli *et al.* (2021). Error bars are expressed as 1 s.

clinopyroxene and garnet was already reported by Weber *et al.* (2002) in two samples of garnet-pyroxene hornblendites. From these observations the authors inferred that quartz should have been present at some point in the initial rock assemblage, but they did not speculate further.

In the arclogite xenoliths of this study, MI occur in garnet from samples 18XC1, 18XC10 and 18XC20, whereas quartz inclusions in garnet are observed in samples 18XC5, 18XC10 and 18XC20. In sample 18XC10, where both inclusion types are most abundant (Fig. 3a,b; Supplementary Fig. S1i), their classical 'zonal arrangement' (Roedder, 1984) demonstrates their primary origin, i.e. that the garnet grew in the presence of both quartz and melt. The lack of quartz in the rest of the xenoliths outside garnet suggests that during or after garnet growth quartz was totally consumed, remaining only as armoured inclusions in garnet. During this process garnet also trapped rutile and zircon crystals.

Fresh or devitrified glass occurs in the xenoliths also along grain boundaries or in thin layers/veinlets. The thinner films coating most grain boundaries (e.g. Fig. 2c) probably represent reaction rims which formed during and after the entrainment of xenoliths in the host lava. Similar features are common in lower crustal xenoliths both at Mercaderes and in other regions (e.g. Hacker *et al.*, 2005). The wider irregular veinlets that crosscut the xenoliths are instead the result of infiltration of the host lava (e.g. Fig. 2a).

The former presence of melt in the xenoliths is also attested by diagnostic microstructures such as plagioclase with crystal faces defining a subhedral shape (Sawyer, 2008; Holness *et al.*, 2011). These microstructures occur in samples 18XC1, 18XC10 and 18XC20 (e.g. Fig. 2b,g) and attest for crystallization of the plagioclase in patches and layers of former melt. This process is compatible with both a cumulitic and a residual origin: in the former case the melt would represent the intercumulus phase, in the latter an anatectic melt.

Melt inclusions often contain sub-micrometric nanolite crystals (Fig. 3h) that represent daughter minerals from the cooling melt. A more detailed discussion on the nanolites can be found in the supplementary Appendix.

Comparison with MI from other tectonic settings

Melt inclusions from Mercaderes were compared with MI from crustal xenoliths of other tectonic settings (i.e. Ichinomegata arc, St. Kitts arc, Bohemian Massif, Neogene Volcanic Province, and Bakony–Balaton Highland Volcanic Field) in order to put some constraints on the formation of felsic melts in the lower crust.

MI observed in sample 18XC1 are low in silica and generally have high concentrations in TiO_2, Al_2O_3, CaO, FeO and MgO, indicating a more 'intermediate' character compared to the MI from the other xenoliths (Fig. 8a-k). Some MI from the St. Kitts arc (Melekhova *et al.*, 2017) and from the Bakony–Balaton Highland Volcanic Field (western Pannonian basin, Hungary; Németh *et al.*, 2021) have also similar low SiO_2 contents, but the other oxides do not share similarities with the MI from Mercaderes. Melts analysed in sample 18XC20 partly overlap the field displayed by the plagioclase-hosted MI from the Ichinomegata arc (Yanagida *et al.*, 2018) for TiO_2, Al_2O_3, Na_2O and K_2O at same SiO_2 contents, but are enriched in FeO and MgO and slightly depleted in CaO and P_2O_5. The SiO_2-rich melts observed in sample 18XC10 are clearly distinct from the MI observed in the Neogene Volcanic Province in Spain which were produced by anatexis of a metapelitic protolith (Cesare *et al.*, 2003; Acosta-Vigil *et al.*, 2007; Ferrero *et al.*, 2011; Bartoli *et al.*, 2016), but share many similarities with the MI from

the Ichinomegata arc (in particular with the magnetite-hosted MI), and from the granulites in SE Pamir (Chupin *et al.*, 2006). The latter, however, have a reverse K_2O/Na_2O ratio. Analogies with MI from the Bohemian Massif (Borghini *et al.*, 2018; Ferrero *et al.*, 2019; Borghini, 2020) are displayed only for Al_2O_3, FeO, MgO, Na_2O and P_2O_5. However, the MI from the Bohemian Massif show a strong depletion in TiO_2 and CaO and a strong enrichment in K_2O compared to the melts measured in the xenoliths from Mercaderes. For what concerns the MI measured in the scapolite crystals of sample 18XC5, they are very similar to the melts from the Bohemian Massif, although the latter are notably depleted in TiO_2 and enriched in K_2O.

The strong enrichment in LILE, the negative Nb–Ta and Ti anomalies, as well as the positive Pb and Sr anomalies consistently displayed by the glasses from the Mercaderes xenoliths are all features typical for subduction-related melts (Fig. 9a–c). The negative Nb–Ta anomalies observed in MI and in the infiltrated melt suggest that rutile and/or ilmenite were part of the partial melting residue or fractionated during crystallization. This is in agreement with the mineral assemblage of the xenoliths, where rutile (sometimes rimmed by ilmenite, see Supplementary Fig. S3) is commonly observed. The positive Sr anomaly of these melts may derive from the partial melting of plagioclase. Sequestration of Nb, Ta and Ti in rutile or ilmenite characterizes also the normalized patterns of the interstitial melt from sample 18XC10, which is interpreted to represent the host lava that percolated into the xenolith. The interstitial melt also shows positive anomalies for Ba and Sr, as well as a weak to moderate negative Eu anomaly $[Eu_N/(Sm_N \cdot Gd_N)^{1/2} = 0.39–0.89]$, with the latter that may indicate early fractionation of plagioclase or retention of plagioclase in the source. Additionally, the positive P anomaly of the interstitial melt also suggests that the host lava was generated from the melting of a phosphorus-bearing phase (likely apatite) present in the source.

Trace element normalized patterns for the melts from Mercaderes are generally enriched compared to MI in migmatitic paragneisses from the Himalaya (Bartoli *et al.*, 2019), with the latter also lacking a negative anomaly for Nb–Ta (Fig. 9b). By contrast, the MI from the Bohemian Massif are strongly enriched in LILE (except for Ba) and Nb–Ta compared to Mercaderes, which, on the other hand, perfectly overlap the pattern displayed by the MI from the Bakony–Balaton Highland Volcanic Field. MI and infiltrated melt from the Mercaderes xenoliths have mantle-normalized trace element patterns that generally lie between the upper crust and lower crust compositions of Rudnick & Gao (2003) but show a slight enrichment in Th–U and a strong depletion in Nb–Ta and Ti. Moreover, the interstitial melt measured in sample 18XC10 displays a strong depletion in middle and heavy rare earth elements, as well as in Ti and Y compared to the upper and lower crust.

Comparison of MI with experimental melts and leucosomes in arcs

Chemical compositions of melt inclusions from Mercaderes were compared with liquids obtained from partial melting experiments of amphibolites between 1.0 and 1.6 GPa (Wolf & Wyllie, 1994; Rapp & Watson, 1995; López & Castro, 2001) and with modelled melt compositions for sample 18XC10, calculated from our phase equilibria modelling with Perple_X (see Fig. 12). Additionally, leucosomes from exhumed arc roots, in particular from the Fiordland arc (Daczko *et al.*, 2001), the Kohistan arc (Garrido *et al.*, 2006), the Amalaoulaou arc (Berger *et al.*, 2011) and the Bougmane arc (Triantafyllou *et al.*, 2018) were also used as references to evaluate the nature of the melts observed in the xenoliths from Mercaderes (see Fig. 9c and Supplementary Fig. S7). In general, from Fig. 12, it is possible to notice that MI from 18XC1 are different compared to the experimental melts, notably in their TiO_2, Al_2O_3 and alkali contents. MI and infiltrated melts analysed in 18XC20 share some similarities with the melts obtained by Wolf & Wyllie (1994) and Rapp & Watson (1995), but are characterized by lower TiO_2 and higher K_2O contents. By contrast, the interstitial melt from sample 18XC20 correlates with the compositions recovered from experiments only for MgO and CaO. In a similar fashion, MI from sample 18XC5 systematically do not overlap (except for TiO_2) the fields displayed by the anatectic experimental melts. Glasses from 18XC10 are comparable to the experimental compositions of Rapp & Watson (1995) at 1.6 GPa and ~1000°C, although the first are slightly richer in CaO and MgO, and poorer in FeO and Na_2O. Furthermore, Fig. 12 also shows that the melt compositions modelled with Perple_X in the predicted stability field of 18XC10, i.e. at 900°C to 1075°C and 1.6 GPa to 1.75 GPa, do not fit with the measured melts. This discrepancy may rely on the fact that the thermodynamic database and solution models used in Perple_X are calibrated only on few experiments and bulk compositions at these P–T conditions.

Compared with leucosomes from exhumed arc roots, which have all been interpreted to result from the partial melting of mafic lithologies (Daczko *et al.*, 2001; Garrido *et al.*, 2006; Berger *et al.*, 2011; Triantafyllou *et al.*, 2018), glasses within the xenoliths from Mercaderes show some differences, both in major and trace elements. In general, MI from 18XC1 have major element compositions that do not correlate with the leucosomes (Supplementary Fig. S7), suggesting that they may not have an anatectic origin. Some glasses from 18XC20 and 18XC10 have similar compositions as leucosomes from the Kohistan arc (although the latter display trends with lower TiO_2 and K_2O, and higher CaO contents), while MI from sample 18XC5 display some analogies as leucosomes from the Bougmane arc, especially for Al_2O_3, FeO and Na_2O (Supplementary Fig. S7).

MI and infiltrated melts within the garnet crystals of the xenoliths have primitive normalized trace element patterns (Fig. 9c) that show some deviations compared to the normalized patterns of the anatectic leucosomes from the Amalaoulaou, the Bougmane and the Fiordland arcs. In particular, the glasses in the MI from the Mercaderes xenoliths are typically more enriched in LILE, Pb, Hf and Zr than the leucosomes from these arcs. On the other hand, leucosomes from the Kohistan paleo-arc are more similar to the patterns displayed by the glasses from Mercaderes, but still show a depletion in Th, U and Hf compared to the latter (Fig. 9c). The interstitial melt from sample 18XC10 has REE normalized patterns similar to those observed for the leucosomes from the Kohistan and Amalaoulaou arc, but displays higher Zr–Hf values compared to the leucosomes.

In general, the comparison of major and trace elements shows that MI and infiltrated melts from samples 18XC10 and 18XC20 are more akin to melts obtained in partial melting experiments of amphibolitic starting materials, and also to anatectic leucosomes from the Kohistan and Amalaoulaou arc sections. MI from sample 18XC5 poorly correlate with experimental melts, but have some similarities with the leucosomes from the Bougmane arc, which have been interpreted to derive from disequilibrium melting of a mafic protolith (Triantafyllou *et al.*, 2018). By contrast, MI from sample 18XC1 have chemical compositions that neither resemble those from partial melting experiments, nor natural anatectic leucosomes, suggesting that sample 18XC1 may have a different origin.

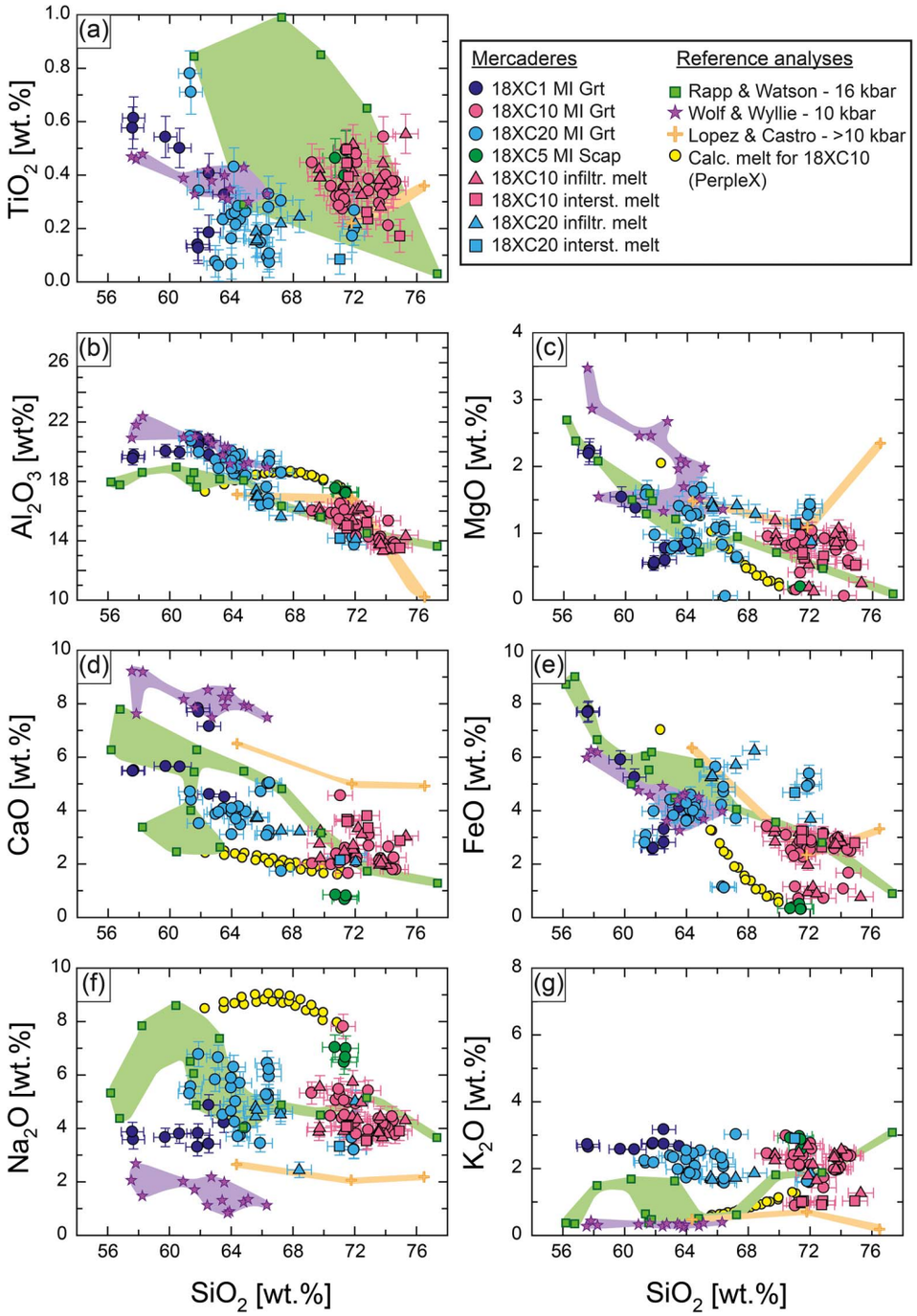

Fig. 12. (a-g) Harker diagrams for the analysed glasses compared with experimental liquids obtained by partial melting of amphibolite starting materials and melts calculated with Perple_X for sample 18XC10. All analyses normalized to 100% on anhydrous basis. Errors on analyses are reported as 2 s.

Origin of the studied arclogites

The chemical composition of the melt entrapped in the primary MI, the latter indicative that the host minerals were growing in the presence of a felsic melt, and a careful evaluation of the microstructures displayed by the different xenoliths allow us to speculate about their origin.

The melt within MI in garnet from samples 18XC10 is rhyolitic in the TAS classification and mostly tonalitic–trondhjemitic in the An–Or–Ab diagram (Supplementary Fig. S4).

Experiments of partial melting of low-K metabasalts (Rapp & Watson, 1995) show that at 1.6 GPa Na-rich trondhjemitic to tonalitic liquids are produced by fluid-absent amphibole melting in the temperature range 1000°C to 1050°C. These low percentage (<10 vol.%) melts coexist with a Grt–Cpx–Amp–Pl ± Qz ± Opx residue in which quartz, amphibole and plagioclase are progressively consumed during heating. The Grt–Cpx-dominated mineralogy of these experimental residues (Rapp & Watson, 1995, their figure 3) is, therefore, compatible with the mineral assemblage

observed in 18XC10. The same conclusion is also supported by other experiments of fluid-absent melting of basaltic amphibolite at 1.0 GPa (Wolf & Wyllie, 1994), as well as at 1.5 and 2.0 GPa (Sen & Dunn, 1994). Hence, the experimental evidence supports the interpretation that arclogitic xenoliths with felsic MI and quartz inclusions in garnet are formed by low-degree partial melting of a (meta)basaltic source, a process that can produce peritectic garnet and clinopyroxene with an anatectic trondhjemitic melt and justify the entrapment of primary felsic MI in garnet. When talking about a (meta)basaltic source, we envisage the rocks constituting the mafic lower crust in arc roots, which may range from igneous textured gabbros, to their metamorphic equivalents dominated by amphibolites and mafic granulites.

Thermodynamic modelling of basaltic compositions also corroborates these results, even though these calculations predict lower temperatures for low degrees of anatexis (800–900°C, Palin *et al.*, 2016; Ducea *et al.*, 2021b). Such thermodynamic simulations were performed using wet basaltic bulk compositions. Also our modelling of the residual composition of sample 18XC10 predicts a solidus at 850°C at 1.6 to 1.8 GPa, and the onset of melting through quartz consumption. All this evidence is in accordance with the general assumption that these types of restitic arclogites in the subarc lower crust derive from the partial melting of underplated (meta)basalts (Lee & Anderson, 2015; Bowman *et al.*, 2021).

Conversely, the silica-rich composition of MI is incompatible with a cumulitic origin of xenoliths like 18XC10, since garnets obtained in high pressure crystallization experiments will not be able to entrap melts with comparable high SiO_2 as in sample 18XC10. Indeed, cumulitic garnet clinopyroxenites are predicted to form primarily by crystallization of basaltic magmas (Green & Ringwood, 1967a, 1967b; Lee & Anderson, 2015 and references therein). Although garnet and clinopyroxene have been observed as liquidus phases of more silicic melts (Carroll & Wyllie, 1990; Alonso-Perez *et al.*, 2009), the andesitic compositions used in these experiments contain >10 wt.% less silica than the MI from sample 18XC10. In addition, none of the above experiments could explain the presence of quartz, found as primary inclusions along with MI, in a growing garnet that eventually could form a cumulate.

Sample 18XC20 is a Hbl + Grt + Pl ± Cpx xenolith characterized by MI with a dacitic/tonalitic compositions (Fig. 7a and Supplementary Fig. S4) and the presence of quartz inclusions in the cores of the garnets. Xenoliths consisting of Hbl + Grt + Pl + Cpx have been also observed in early Miocene high-silica andesites and dacites from the Northland Peninsula (New Zealand). These xenoliths have been interpreted to be cognate, i.e. directly crystallized form the host calc-alkaline lavas (Day *et al.*, 1992). Further experimental studies on H_2O-bearing dacites (3–5 wt.% H_2O) from the Northland Peninsula have shown that at P > 1.3 GPa Grt and Cpx can be liquidus phases, and that Qz and Amp (ferroan pargasite to edenitic hornblende) appear together, while Cpx disappears, at T < 920–900°C (Green, 1992). Although we do not disregard the possibility that 18XC20 might have a cumulitic origin after fractional crystallization of a dacitic melt, the presence of quartz inclusions associated to primary melt inclusions solely in the garnet cores, and not in the matrix of the xenolith, points more towards a restitic formation and the conclusions derived from 18XC10 seem to be valid also for 18XC20.

The melt entrapped in the MI found in scapolite from sample 18XC5 is rhyolitic (Fig. 7a) and fall well within the trondhjemitic field of the An–Or–Ab diagram (Supplementary Fig. S4). MI in scapolite have been also noticed in granulitic xenoliths from diatremes in southeastern Pamir (Tajikistan), which were interpreted to be the result of incongruent partial melting of lower crustal lithologies at P > 1.3 GPa and T ~ 1000°C (Chupin *et al.*, 2006). Similar P–T conditions have been determined by geothermobarometry also for sample 18XC5. Additionally, considering the rhyolitic composition of the MI and the presence of Qz inclusions in the garnets, it can be inferred that 18XC5 may have also been formed after incongruent partial melting of a metabasaltic lithology.

Sample 18XC1 shows significant differences with respect to the other three arclogites: a greater abundance of plagioclase and amphibole, the lack of quartz inclusions in garnet, and the (trachy)andesitic composition of MI in garnet. Even though straightforward textures are not observed, these features could be more compatible with a cumulate origin rather than with a restitic one. The mineral assemblage may in fact be produced by the crystallization of an andesitic melt with moderate H_2O contents at P > 1 GPa (Alonso-Perez *et al.*, 2009), and the 18XC1 arclogite could represent a cumulate after this process. This interpretation is also corroborated by the less evolved composition of the glass measured in the MI, which is not consistent with melts from partial melting experiments and natural anatectic leucosomes (see above). The H_2O content in the MI of about 2.0 ± 1.0 wt.% (s.e.m.), for sample 18XC1 would passively increase during crystallization of garnet and clinopyroxene, and be partly used for the later crystallization of amphibole. The density for sample 18XC1, calculated from its modal assemblage, is 3.23 g/cm^3.

Combining the textural, chemical and thermobarometric constraints provided in this study, we propose that the arclogite xenoliths that contain primary MI and quartz inclusions in garnet represent restites after the re-melting of a mafic, Qz-bearing protolith. This conclusion is supported in particular by sample 18XC10, where the genetic constraints are best evident. The re-melting of a mafic crust produced a Grt-Cpx-rich residue with minor plagioclase and amphibole, and progressively consumed quartz that must have been present in the protolith and is preserved only as inclusions in the cores of garnet. In order to produce a silica-rich trondhjemitic anatectic melt, the degree of melting was low (Rapp & Watson, 1995). Similar conclusions seem to be valid also for samples 18XC5 and 18XC20.

Therefore, we provide evidence for the presence of both cumulitic and restitic arclogites in the lower portion of the active Colombian volcanic arc.

The arclogites equilibrated at temperature of 960 to 1150°C and pressure of ~1.6 to 2.0 GPa, corresponding to a depth of 60 to 75 km in the arc root assuming a crustal density of 2.7 g/cm^3. The thermobarometric estimates obtained for our samples fit with the P–T array defined by the crustal xenoliths from Mercaderes studied by Bloch *et al.* (2017), which should represent the present-day geotherm in the arc region. Our results are also consistent with new geophysical investigations, that infer a crustal thickness of 64.5 to 72.5 km for the Colombian volcanic arc (Avellaneda-Jiménez & Monsalve, 2022). The anomalously high P–T conditions calculated for rim (3.0 GPa, 1400°C) and core (2.0 GPa, 1260°C) of a Grt-Cpx pair in sample 18XC1 may indicate that the two minerals were not in chemical equilibrium, and therefore, these results have been excluded for further discussions on the equilibration conditions of this xenolith.

Sample 18XC10 is a typical low MgO (10.2 wt.%), low X_{Mg} (0.58) pyroxenite in the distinction of Lee & Anderson (2015). Its density, calculated from its chemical and modal composition, is >3.4 g/cm^3 as expected from low MgO arclogites (Lee & Anderson, 2015; Ducea *et al.*, 2021a, 2021b) and confirms that this rock is negatively buoyant relative to the upper mantle and has the

potential for foundering/delamination from the arc roots (Bloch *et al.*, 2017).

Unlike other xenoliths at Mercaderes (Weber *et al.*, 2002), sample 18XC10 shows very little evidence of reaction rims and growth of secondary amphibole at grain boundaries. In addition, both garnet and clinopyroxene grains are compositionally homogeneous. These features, also observed in earlier studies (Weber *et al.*, 2002; Bloch *et al.*, 2017), indicate that part of the xenoliths, including 18XC10, were in P–T equilibrium in the region of residence at the time of entrapment in the host magma, and their assemblages were not affected by the ascent toward the surface or to shallower depths prior to eruption.

Potentials of elastic thermobarometry

Pressure–temperature conditions for arclogites from the literature typically describe a wide field between 700–950°C and 1.0–3.0 GPa (e.g. California; Ducea & Saleeby, 1996; central Arizona, Rautela *et al.*, 2020). Arclogites from Mercaderes suggest instead a much higher equilibration temperature of about 1100 to 1200°C, which has been linked to crustal foundering (Bloch *et al.*, 2017).

Classical geothermobarometric techniques coupled with thermodynamic modelling for the mineral assemblage of sample 18XC10 suggest the rock formed from partial melting at P–T conditions of ~1050 ± 100°C (2 s.e.m.) and 1.5 to 1.8 GPa. These conditions agree with the Fe-Mg order–disorder thermometry on clinopyroxene, which records an average closure temperature of 1090 ± 30°C (2 s.e.m.) and are, therefore, consistent with the partial melting of a lower arc (meta)basaltic rock at H_2O-undersaturated conditions. Moreover, our results fall along the geothermal gradient defined by Bloch *et al.* (2017) for the Mercaderes area (Fig. 10b).

Elastic geothermobarometry of quartz and zircon inclusion in garnet suggest higher P–T conditions of 1150 ± 30°C (2 s.e.m.) and 1.9 ± 0.2 GPa (2 s.e.m.). Results of elastic geobarometry can provide pressure and temperature conditions of inclusion entrapment within a mineral host. However, examples of non-elastic processes in inclusion–host systems are numerous (e.g. Campomenosi *et al.*, 2021). Also, post-entrapment shape maturation of quartz within garnet might also affect the elastic behaviour of the system (Cesare *et al.*, 2021). Recent experimental investigations on zircon inclusion in garnet (Campomenosi *et al.*, 2022) showed that non-elastic re-equilibration of host-inclusion system is P–T path-rather than temperature-dependent. Such mechanical resetting occurs when a zircon in garnet, after entrapment, is heated to temperatures greater than those of entrapment, or is decompressed isothermally (Campomenosi *et al.*, 2021, 2022). The zircon-in-garnet host-inclusion system thus records the maximum temperature at the lowest pressure reached by the system. Therefore, we propose that zircon inclusions in sample 18XC10 were entrapped, along with quartz and melt inclusions, at ~1050°C, 1.5–1.8 GPa, and were then plastically reset at 1150°C and 1.9 ± 0.2 (2 s.e.m.) GPa. Quartz-in-garnet geobarometry is consistent with both the P–T conditions suggested by thermodynamic modelling and by zircon-in-garnet geobarometry. Shape maturation mechanisms of quartz at high temperature which lead to inclusion faceting (see Fig. 3k) might be related to non-elastic reset (Cesare *et al.*, 2021), but clear experimental proofs are still lacking. Since it is unknown whether quartz undergoes a non-elastic reset similarly to zircon, it is unclear whether this isomeke records the entrapment conditions during partial melting or the plastic reset at higher temperature.

Sample 18XC10 might, therefore, support the hypothesis of crustal foundering in the Mercaderes-Río Mayo area, because by looking at the absolute values of its possible P–T path, one can notice that the sample displays a prograde heating path from 1050°C and 1.6 GPa to 1150°C and 1.9 GPa. However, we also recognize that, due to the high error on the Fe-Mg exchange geothermobarometers, the conclusion that sample 18XC10 shows foundering at the mineral grain scale should be taken with care.

Tectonic implications

The Mercaderes area is a rare, if not the unique, example where both residues from partial melting of metabasalts and cumulates from the high-pressure crystallization of basaltic/andesitic mantle-derived liquids along an active Cordilleran margin can be directly observed. This corroborates the idea that these two (apparently) antithetic rock-forming processes can occur in a single setting such as the lower arc crust (Bowman *et al.*, 2021), especially in mature arcs, where the crustal section may exceed 50 km in thickness.

The interplay between lower crust anatexis and crystallization of mantle-derived melts, both leading to the formation of dense mafic arclogites, has important implications for the formation and geochemical evolution of volcanic arcs. A first possible consequence is that the dacitic to rhyolitic melts produced during the partial melting of metabasaltic protoliths may interact and hybridize the primitive basalts derived by the partial melting of the mantle (see Fig. 13). Such a process might justify part of the crustal signature observed in many granitic batholiths and which has been typically related to the crustal assimilation of the surrounding country rock (e.g. DePaolo, 1981; Ague & Brimhall, 1987). Secondly, the formation of arclogites (both cumulates or restites) denser than the underlying lithospheric mantle implies a physical instability of the arc root (Lee & Anderson, 2015; Bowman *et al.*, 2021; Ducea *et al.*, 2021a, 2021b), with arclogites that undergo foundering into the mantle and eventually may delaminate (complete detachment from the base of the arc). Density sorting in lower arc roots has been suggested to be one of the major mechanisms that drives arc magmas towards high silica contents and consequently towards a bulk arc crust more akin to an andesitic continental crust (e.g. Jagoutz & Behn, 2013; Jagoutz & Schmidt, 2013; Ducea *et al.*, 2021b). The density calculated for sample 18XC10 is 4% to 7% higher than that of the lithospheric mantle (assuming a density of 3.30 ± 0.05 g/cm^3), consistent with the values estimated by Bloch *et al.* (2017) for some Grt-clinopyroxenites from the same region. Therefore, it seems plausible that, as suggested by Bloch *et al.* (2017), the lower continental crust between the Colombian Western and Central Cordilleras is currently subjected to foundering into the lithospheric mantle. However, Bowman *et al.* (2021) have shown that the process of foundering is strongly dependent on the amount of the melt in equilibrium with the residues that is retained by the system. For melt volumes lower than 10 to 18 vol.%, it is suggested that the arclogites are prone to founder, while at higher melt volumes they are stabilized in the arc root. Furthermore, it is also inferred that the arclogites may be partially re-melted, while sinking into the mantle, favouring its re-fertilization (Bowman *et al.*, 2021; Ducea *et al.*, 2021b). The melting behaviour of the foundering arclogites will ultimately depend on the regional geotherm and hotter geotherms will produce larger amounts of melt than colder ones. As a consequence, and in analogy to what proposed by Bowman *et al.* (2021), the tendency to sink for this crustal blob will be inversely proportional to the amount of melt present in the system (since this melt has a much lower density), with 'drained' blobs that will have the highest tendency to continue along their

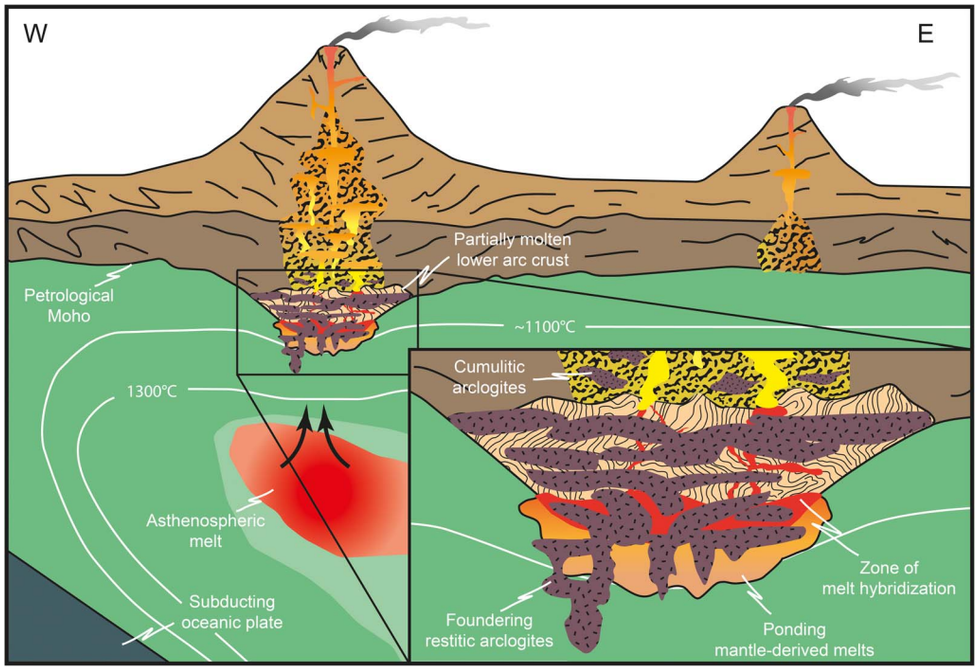

Fig. 13. Schematic cartoon (not to scale) showing the formation of cumulitic and restitic arclogites in the lower arc crust and the development of hybrid melts.

sinking trajectory. This hypothesis was tested by monitoring the supra-solidus density evolution of sample 18XC10 along three geotherms (500°C/GPa, 600°C/GPa and 640°C/GPa) that intersect and bound the stability field of the rock estimated by Perple_X, and along the geotherm of 720°C/GPa determined by Bloch *et al.* (2017) for the Mercaderes area (see Fig. 10a). Within the P–T field calculated by Perple_X it is possible to notice that the total density of the system (residue + melt) decreases with increasing degree of melting, while the density of the residue increases (see Supplementary Fig. S8 and Supplementary Table S7). As expected, the largest variations in density, both for the total system and the residue, are displayed along the hotter geotherms. This implies that the effective sinking of a partially molten rock similar to sample 18XC10 depends on the amount of melt that is retained in it, with the consequence that at high melt volumes the blob may reach a neutral buoyancy with the surrounding mantle and pond. On the other hand, if some of the melt is released during the descent of the blob, then the density is predominantly governed by the density of the solid residue, leading to a negative buoyancy of the crustal blob.

CONCLUSIONS

The roots of volcanic continental and oceanic arcs are important interfaces where major exchanges of mass between mantle and crust occur. Arc roots are characterized by a dual nature, in which high pressure crystallization and partial melting play a fundamental role in the formation and evolution of the bulk arc crust. Cumulates and restites resulting from these two distinct processes have similar mineral assemblages, thus making any unambiguous inference on their origin very difficult. Additionally, field evidence for re-melting of mafic orthogneisses and/or amphibolites within volcanic arcs has been reported to be limited and equivocal (Jagoutz & Klein, 2018). Nevertheless, in our study we could demonstrate that a careful petrographical and microstructural investigation of mineral and melt inclusions and their geochemical characterization may help in the discrimination of the two endmembers. In particular, the concomitant presence of quartz inclusions closely associated to MI in the garnet cores of the investigated xenoliths has been interpreted to be diagnostic for restitic arclogites. Although we cannot, and do not want to, speculate on the relative importance of cumulus versus re-melting processes for the origin of arclogites, our study provides the first field-based evidence that some arclogite xenoliths from Mercaderes-Río Mayo are residues after partial melting of a metabasaltic crust, suggesting also that the occurrence of magmatic cumulates and anatectic restites may be concomitant, especially in mature arcs, where the arc root has a considerable thickness. It is also proposed that the thick root of mature arcs is a more favourable zone for melt hybridization and delamination of dense residues compared to the root of thin arcs.

Supplementary Data

Supplementary data are available at *Journal of Petrology* online.

ACKNOWLEDGEMENTS

We thank Leonardo Tauro for the preparation of high quality polished thin sections, Federico Zorzi for his assistance at CEASC and Andrea Risplendente for his invaluable help during electron microprobe analyses. Chiara Groppo is thanked for the acquisition of SEM maps. O.G. thanks Marco Agustoni for the help with the *Metas.UncLib* Python script. We acknowledge funding from Italian MUR (grants PRIN 2017ZE49E7 to B.C. and PRIN 202037YPCZ_001 to M.P.). M.A. and M.G. have been partially supported by the PRIN-MUR project 'THALES' Prot.2020WPMFE9_003 and by the Highlight funded by Fondi regione Lombardia DGR 3776. Benjamin Urann

and an anonymous reviewer are thanked for their constructive reviews. Adam Kent is thanked for editorial handling.

AQ9

References

Acosta-Vigil, A., London, D., Morgan, G. B. & Dewers, T. A. (2003). Solubility of excess alumina in hydrous granitic melts in equilibrium with peraluminous minerals at 700–800 °C and 200 MPa, and applications of the aluminum saturation index. *Contributions to Mineralogy and Petrology* **146**, 100–119. https://doi.org/10.1007/s00410-003-0486-6.

Acosta-Vigil, A., Cesare, B., London, D. & Morgan, G. B. (2007). Microstructures and composition of melt inclusions in a crustal anatectic environment, represented by metapelitic enclaves within El Hoyazo dacites, SE Spain. *Chemical Geology* **237**, 450–465. https://doi.org/10.1016/j.chemgeo.2006.07.014.

Ague, J. J. & Brimhall, G. H. (1987). Granites of the batholiths of California: products of local assimilation and regional-scale crustal contamination. *Geology* **15**, 63–66. https://doi.org/10.1130/0091-7613(1987)15<63:GOTBOC>2.0.CO;2.

Alonso-Perez, R., Müntener, O. & Ulmer, P. (2009). Igneous garnet and amphibole fractionation in the roots of island arcs: experimental constraints on andesitic liquids. *Contributions to Mineralogy and Petrology* **157**, 541–558. https://doi.org/10.1007/s00410-008-0351-8.

Angel, R. J., Mazzucchelli, M. L., Alvaro, M., Nimis, P. & Nestola, F. (2014). Geobarometry from host-inclusion systems: the role of elastic relaxation. *American Mineralogist* **99**, 2146–2149. https://doi.org/10.2138/am-2014-5047.

Angel, R. J., Alvaro, M., Miletich, R. & Nestola, F. (2017a). A simple and generalised P–T–V EoS for continuous phase transitions, implemented in EosFit and applied to quartz. *Contributions to Mineralogy and Petrology* **172**, 1–15. https://doi.org/10.1007/s00410-017-1349-x.

Angel, R. J., Mazzucchelli, M. L., Alvaro, M. & Nestola, F. (2017b). EosFit-Pinc: a simple GUI for host-inclusion elastic thermobarometry. *American Mineralogist* **102**, 1957–1960. https://doi.org/10.2138/am-2017-6190.

Angel, R. J., Murri, M., Mihailova, B. & Alvaro, M. (2019). Stress, strain and Raman shifts. *Zeitschrift für Kristallographie-Crystalline Materials* **234**, 129–140. https://doi.org/10.1515/zkri-2018-2112.

Angel, R. J., Gilio, M., Mazzucchelli, M. & Alvaro, M. (2022). Garnet EoS: a critical review and synthesis. *Contributions to Mineralogy and Petrology* **177**, 1–22. https://doi.org/10.1007/s00410-022-01918-5.

Avellaneda-Jiménez, D. S. & Monsalve, G. (2022). Arclogite nature of the Colombian Andes magmatic arc root: a receiver-function approach. *Tectonophysics* **836**, 229417–229410. https://doi.org/10.1016/j.tecto.2022.229417.

Bartoli, O., Acosta-Vigil, A., Ferrero, S. & Cesare, B. (2016). Granitoid magmas preserved as melt inclusions in high-grade metamorphic rock. *American Mineralogist* **101**, 1543–1559. https://doi.org/10.2138/am-2016-5541CCBYNCND.

Bartoli, O., Acosta-Vigil, A., Cesare, B., Remusat, L., Gonzalez-Cano, A., Wälle, M., Tajčmanová, L. & Langone, A. (2019). Geochemistry of Eocene-Early Oligocene low-temperature crustal melts from Greater Himalayan sequence (Nepal): a nanogranitoid perspective. *Contribution to Mineralogy and Petrology* **174**, 1–18. https://doi.org/10.1007/s00410-019-1622-2.

Behrens, H. & Jantos, N. (2001). The effect of anhydrous composition on water solubility in granitic melts. *American Mineralogist* **86**, 14–20. https://doi.org/10.2138/am-2001-0102.

Berger, J., Caby, R., Liégeois, J. P., Mercier, J. C. C. & Demaiffe, D. (2011). Deep inside a neoproterozoic intra-oceanic arc: growth, differentiation and exhumation of the Amalaoulaou complex (Gourma, Mali). *Contributions to Mineralogy and Petrology* **162**, 773–796. https://doi.org/10.1007/s00410-011-0624-5.

Beyer, C., Frost, D. J. & Miyajima, N. (2015). Experimental calibration of a garnet–clinopyroxene geobarometer for mantle eclogites. *Contributions to Mineralogy and Petrology* **169**, 1–21. https://doi.org/10.1007/s00410-015-1113-z.

Binvignat, F. A. P., Malcherek, T., Angel, R. J., Paulmann, C., Schlüter, J. & Mihailova, B. (2018). Radiation-damaged zircon under high pressures. *Physics and Chemistry of Minerals* **45**, 981–993. https://doi.org/10.1007/s00269-018-0978-6.

Bloch, E., Ibañez-Mejia, M., Murray, K., Vervoort, J. & Müntener, O. (2017). Recent crustal foundering in the northern volcanic zone of the Andean arc: petrological insights from the roots of a modern subduction zone. *Earth and Planetary Science Letters* **476**, 47–58. https://doi.org/10.1016/j.epsl.2017.07.041.

Borghini, A. (2020). Melt inclusions in mafic rocks as witnesses of metasomatism in the Bohemian Massif. PhD diss. *Universität Potsdam* **2020**, 1–205.

Borghini, A., Ferrero, S., Wunder, B., Laurent, O., O'Brien, P. J. & Ziemann, M. A. (2018). Granitoid melt inclusions in orogenic peridotite and the origin of garnet clinopyroxenite. *Geology* **46**, 1007–1010. https://doi.org/10.1130/G45316.1.

Bowman, E. E., Ducea, M. N. & Triantafyllou, A. (2021). Arclogites in the subarc lower crust: effects of crystallization, partial melting, and retained melt on the foundering ability of residual roots. *Journal of Petrology* **62**, 1–22. https://doi.org/10.1093/petrology/egab094.

Brizi, E., Molin, G. & Zanazzi, P. F. (2000). Experimental study of intracrystalline Fe^{2+}-mg exchange in three augite crystals: effect of composition on geothermometric calibration. *American Mineralogist* **85**, 1375–1382. https://doi.org/10.2138/am-2000-1005.

Burg, J. P. (2011) The Asia–Kohistan–India collision: review and discussion. In: *Arc-continent collision*. Berlin, Heidelberg: Springer, pp.279–309.

Campomenosi, N., Rubatto, D., Hermann, J., Mihailova, B., Scambelluri, M. & Alvaro, M. (2020). Establishing a protocol for the selection of zircon inclusions in garnet for Raman thermobarometry. *American Mineralogist* **105**, 992–1001. https://doi.org/10.2138/am-2020-7246.

Campomenosi, N., Scambelluri, M., Angel, R. J., Hermann, J., Mazzucchelli, M. L., Mihailova, B., Piccoli, F. & Alvaro, M. (2021). Using the elastic properties of zircon-garnet host-inclusion pairs for thermobarometry of the ultrahigh-pressure Dora-Maira whiteschists: problems and perspectives. *Contributions to Mineralogy and Petrology* **176**, 1–17. https://doi.org/10.1007/s00410-021-01793-6.

Campomenosi, N., Angel, R. J., Alvaro, M. & Mihailova, B. (2022). Resetting of zircon inclusions in garnet: implications for elastic thermobarometry. *Geology* , 1–5.

Carroll, M. R. & Wyllie, P. J. (1990). The system tonalite-H_2O at 15 kbar and the genesis of calc-alkaline magmas. *American Mineralogist* **75**, 345–357.

Cesare, B., Marchesi, C., Hermann, J. & Gómez-Pugnaire, M. T. (2003). Primary melt inclusions in andalusite from anatectic graphitic metapelites: implications for the position of the Al_2SiO_5 triple point. *Geology* **31**, 573–576. https://doi.org/10.1130/0091-7613(2003)031<0573:PMIIAF>2.0.CO;2.

Cesare, B., Parisatto, M., Mancini, L., Peruzzo, L., Franceschi, M., Tacchetto, T., Reddy, S., Spiess, R., Nestola, F. & Marone, F. (2021). Mineral inclusions are not immutable: evidence of post-entrapment thermally-induced shape change of quartz in

garnet. *Earth and Planetary Science Letters* **555**, 116708. https://doi.org/10.1016/j.epsl.2020.116708.

Chupin, V. P., Kuz'min, D. V. & Madyukov, I. A. (2006). Melt inclusions in minerals of scapolite-bearing granulite (lower crustal xenoliths from diatremes of the Pamirs). *Doklady Earth Sciences* **407**, 507–511. https://doi.org/10.1134/S1028334X06030366.

Connolly, J. A. (2005). Computation of phase equilibria by linear programming: a tool for geodynamic modeling and its application to subduction zone decarbonation. *Earth and Planetary Science Letters* **236**, 524–541. https://doi.org/10.1016/j.epsl.2005.04.033.

Connolly, J. A. D. (2009). The geodynamic equation of state: what and how. *Geochemistry, Geophysics, Geosystems* **10**, 1–19. https://doi.org/10.1029/2009GC002540.

Daczko, N. R., Clarke, G. L. & Klepeis, K. A. (2001). Transformation of two-pyroxene hornblende granulite to garnet granulite involving simultaneous melting and fracturing of the lower crust, Fiordland, New Zealand. *Journal of Metamorphic Geology* **19**, 549–562. https://doi.org/10.1046/j.0263-4929.2001.00328.x.

Day, R. A., Green, T. H. & Smith, I. E. M. (1992). The origin and significance of garnet phenocrysts and garnet-bearing xenoliths in Miocene calc-alkaline volcanics from northland, New Zealand. *Journal of Petrology* **33**, 125–161. https://doi.org/10.1093/petrology/33.1.125.

DeBari, S. M. & Greene, A. R. (2011) Vertical stratification of composition, density, and inferred magmatic processes in exposed arc crustal sections. In: *Arc-continent collision*. Berlin, Heidelberg: Springer, pp.121–144.

DePaolo, D. J. (1981). Trace element and isotopic effects of combined wallrock assimilation and fractional crystallization. *Earth and Planetary Science Letters* **53**, 189–202. https://doi.org/10.1016/0012-821X(81)90153-9.

Domeneghetti, M. C., Fioretti, A. M., Cámara, F., McCammon, C. & Alvaro, M. (2013). Thermal history of nakhlites: a comparison between MIL 03346 and its terrestrial analogue Theo's flow. *Geochimica et Cosmochimica Acta* **121**, 571–581. https://doi.org/10.1016/j.gca.2013.07.044.

Ducea, M. N. & Saleeby, J. B. (1996). Buoyancy sources for a large, unrooted mountain range, the Sierra Nevada, California: evidence from xenolith thermobarometry. *Journal of Geophysical Research: Solid Earth* **101**, 8229–8244. https://doi.org/10.1029/95JB03452.

Ducea, M. N., Otamendi, J. E., Bergantz, G. W., Jianu, D. & Petrescu, L. (2015). The origin and petrologic evolution of the Ordovician Famatinian-Puna arc. *Geological Society of America Memoirs* **212**, 125–138. https://doi.org/10.1130/2015.1212(07).

Ducea, M. N., Chapman, A. D., Bowman, E. & Triantafyllou, A. (2021a). Arclogites and their role in continental evolution; part 1: background, locations, petrography, geochemistry, chronology and thermobarometry. *Earth-Science Reviews* **214**, 103375. https://doi.org/10.1016/j.earscirev.2020.103375.

Ducea, M. N., Chapman, A. D., Bowman, E. & Balica, C. (2021b). Arclogites and their role in continental evolution; part 2: relationship to batholiths and volcanoes, density and foundering, remelting and long-term storage in the mantle. *Earth-Science Reviews* **214**, 103476. https://doi.org/10.1016/j.earscirev.2020.103476.

Ehlers, A. M., Zaffiro, G., Angel, R. J., Boffa-Ballaran, T., Carpenter, M. A., Alvaro, M. & Ross, N. L. (2022). Thermoelastic properties of zircon: implications for geothermobarometry. *American Mineralogist* **107**, 74–81. https://doi.org/10.2138/am-2021-7731.

Ferrero, S., Bodnar, R. J., Cesare, B. & Viti, C. (2011). Re-equilibration of primary fluid inclusions in peritectic garnet from metapelitic enclaves, El Hoyazo, Spain. *Lithos* **124**, 117–131. https://doi.org/10.1016/j.lithos.2010.09.004.

Ferrero, S., O'Brien, P. J., Borghini, A., Wunder, B., Wälle, M., Günter, C. & Ziemann, M. A. (2019). A treasure chest full of nanogranitoids: an archive to investigate crustal melting in the bohemian massif. *Geological Society, London, Special Publications* **478**, 13–38. https://doi.org/10.1144/SP478.19.

Ganguly, J. (1982). Mg-Fe order-disorder in ferromagnesian silicates: II. Thermodynamics, kinetics, and geological applications. *Journal of Environmental Sciences (China) English Ed* , 58–99.

Garrido, C. J., Bodinier, J. L., Burg, J. P., Zeilinger, G., Hussain, S. S., Dawood, H., Nawaz Chaudhry, M. & Gervilla, F. (2006). Petrogenesis of mafic garnet granulite in the lower crust of the Kohistan paleo-arc complex (Northern Pakistan): implications for intra-crustal differentiation of island arcs and generation of continental crust. *Journal of Petrology* **47**, 1873–1914. https://doi.org/10.1093/petrology/egl030.

Green, T. H. (1992). Experimental phase equilibrium studies of garnet-bearing I-type volcanics and high-level intrusives from northland, New Zealand. *Earth and Environmental Science Transactions of the Royal Society of Edinburgh* **83**, 429–438. https://doi.org/10.1017/S0263593300008105.

Green, D. H. & Ringwood, A. E. (1967a). The genesis of basaltic magmas. *Contributions to Mineralogy and Petrology* **15**, 103–190. https://doi.org/10.1007/BF00372052.

Green, D. H. & Ringwood, A. E. (1967b). An experimental investigation of the gabbro to eclogite transformation and its petrological applications. *Geochimica et Cosmochimica Acta* **31**, 767–833. https://doi.org/10.1016/S0016-7037(67)80031-0.

Green, E. C. R., White, R. W., Diener, J. F. A., Powell, R., Holland, T. J. B. & Palin, R. M. (2016). Activity–composition relations for the calculation of partial melting equilibria in metabasic rocks. *Journal of Metamorphic Geology* **34**, 845–869. https://doi.org/10.1111/jmg.12211.

Greene, A. R., DeBari, S. M., Kelemen, P. B., Blusztajn, J. & Clift, P. D. (2006). A detailed geochemical study of island arc crust: the Talkeetna Arc section, south-central Alaska. *Journal of Petrology* **47**, 1051–1093. https://doi.org/10.1093/petrology/egl002.

Hacker, B., Luffi, P., Lutkov, V., Minaev, V., Ratschbacher, L., Plank, T., Ducea, M., Patiño-Douce, A., McWilliams, M. & Metcalf, J. (2005). Near-ultrahigh pressure processing of continental crust: Miocene crustal xenoliths from the Pamir. *Journal of Petrology* **46**, 1661–1687. https://doi.org/10.1093/petrology/egi030.

Hacker, B. R., Kelemen, P. B. & Behn, M. D. (2011). Differentiation of the continental crust by relamination. *Earth and Planetary Science Letters* **307**, 501–516. https://doi.org/10.1016/j.epsl.2011.05.024.

Hacker, B. R., Kelemen, P. B. & Behn, M. D. (2015). Continental lower crust. *Annual Review of Earth and Planetary Sciences* **43**, 167–205. https://doi.org/10.1146/annurev-earth-050212-124117.

Holland, T. & Powell, R. (2003). Activity–composition relations for phases in petrological calculations: an asymmetric multicomponent formulation. *Contributions to Mineralogy and Petrology* **145**, 492–501. https://doi.org/10.1007/s00410-003-0464-z.

Holness, M. B., Cesare, B. & Sawyer, E. W. (2011). Melted rocks under the microscope: microstructures and their interpretation. *Elements* **7**, 247–252. https://doi.org/10.2113/gselements.7.4.247.

Holtz, F., Johannes, W., Tamic, N. & Behrens, H. (2001). Maximum and minimum water contents of granitic melts generated in the crust: a reevaluation and implications. *Lithos* **56**, 1–14. https://doi.org/10.1016/S0024-4937(00)00056-6.

Ingamells, C. O. (1978). Analyzed minerals for electron microprobe standards. *Geostandards Newsletter* **2**, 115. https://doi.org/10.1111/j.1751-908X.1978.tb00216.x.

Jagoutz, O. & Behn, M. D. (2013). Foundering of lower island-arc crust as an explanation for the origin of the continental Moho. *Nature* **504**, 131–134. https://doi.org/10.1038/nature12758.

Jagoutz, O. & Kelemen, P. B. (2015). Role of arc processes in the formation of continental crust. *Annual Review of Earth and Planetary Sciences* **43**, 363–404. https://doi.org/10.1146/annurev-earth-040809-152345.

Jagoutz, O. & Klein, B. (2018). On the importance of crystallization-differentiation for the generation of SiO_2-rich melts and the compositional build-up of arc (and continental) crust. *American Journal of Science* **318**, 29–63. https://doi.org/10.2475/01.2018.03.

Jagoutz, O. & Schmidt, M. W. (2012). The formation and bulk composition of modern juvenile continental crust: the Kohistan arc. *Chemical Geology* **298-299**, 79–96. https://doi.org/10.1016/j.chemgeo.2011.10.022.

Jagoutz, O. & Schmidt, M. W. (2013). The composition of the foundered complement to the continental crust and a re-evaluation of fluxes in arcs. *Earth and Planetary Science Letters* **371-372**, 177–190. https://doi.org/10.1016/j.epsl.2013.03.051.

Jarosewich, E. (2002). Smithsonian microbeam standards. *Journal of Research of the National Institute of Standards and Technology* **107**, 681–685. https://doi.org/10.6028/jres.107.054.

Jarosewich, E., Nelen, J. A. & Norberg, J. A. (1980). Reference samples for electron microprobe analysis. *Geostandards Newsletter* **4**, 43–47. https://doi.org/10.1111/j.1751-908X.1980.tb00273.x.

Kelemen, P. B. & Behn, M. D. (2016). Formation of lower continental crust by relamination of buoyant arc lavas and plutons. *Nature Geoscience* **9**, 197–205. https://doi.org/10.1038/ngeo2662.

Kelemen, P. B., Hanghøj, K. & Greene, A. R. (2014) One view of the geochemistry of subduction-related magmatic arcs, with an emphasis on primitive andesite and lower crust. In: Holland H. D. & Turekian K. K. (eds) *Treatise on Geochemistry*, Vol. 3, 2nd edn. Amsterdam: Elsevier, pp.749–806.

Klein, B. Z. & Jagoutz, O. (2021). Construction of a trans-crustal magma system: building the Bear Valley Intrusive Suite, southern Sierra Nevada. *Earth and Planetary Science Letters* **553**, 116624. https://doi.org/10.1016/j.epsl.2020.116624.

Kuzmany, H. (2009) *Solid-state spectroscopy: an introduction*. Berlin: springer, p.554.

Le Bas, M. J., Le Maitre, R. W., Streckeisen, A. & Zanettin, A. (1986). A chemical classification of volcanic rocks based on the total alkali-silica diagram. *Journal of Petrology* **27**, 745–750. https://doi.org/10.1093/petrology/27.3.745.

Lee, C. T. A. & Anderson, D. L. (2015). Continental crust formation at arcs, the arclogite "delamination" cycle, and one origin for fertile melting anomalies in the mantle. *Science Bulletin* **60**, 1141–1156. https://doi.org/10.1007/s11434-015-0828-6.

Lee, C. T. A., Cheng, X. & Horodyskyj, U. (2006). The development and refinement of continental arcs by primary basaltic magmatism, garnet pyroxenite accumulation, basaltic recharge and delamination: insights from the Sierra Nevada, California. *Contributions to Mineralogy and Petrology* **151**, 222–242. https://doi.org/10.1007/s00410-005-0056-1.

López, S. & Castro, A. (2001). Determination of the fluid–absent solidus and supersolidus phase relationships of MORB-derived amphibolites in the range 4–14 kbar. *American Mineralogist* **86**, 1396–1403. https://doi.org/10.2138/am-2001-11-1208.

Makhluf, A. R., Newton, R. C. & Manning, C. E. (2017). Experimental determination of liquidus H_2O contents of haplogranite at deep-crustal conditions. *Contributions to Mineralogy and Petrology* **172**, 1–18. https://doi.org/10.1007/s00410-017-1392-7.

Mazzucchelli, M. L., Burnley, P., Angel, R. J., Morganti, S., Domeneghetti, M. C., Nestola, F. & Alvaro, M. (2018). Elastic geothermobarometry: corrections for the geometry of the host-inclusion system. *Geology* **46**, 231–234. https://doi.org/10.1130/G39807.1.

Mazzucchelli, M. L., Angel, R. J. & Alvaro, M. (2021). EntraPT: an online platform for elastic geothermobarometry. *American Mineralogist* **106**, 830–837. https://doi.org/10.2138/am-2021-7693CCBYNCND.

McDonough, W. F. & Sun, S. S. (1995). The composition of the earth. *Chemical Geology* **120**, 223–253. https://doi.org/10.1016/0009-2541(94)00140-4.

Melekhova, E., Blundy, J., Martin, R., Arculus, R. & Pichavant, M. (2017). Petrological and experimental evidence for differentiation of water-rich magmas beneath St. Kitts, Lesser Antilles. *Contributions to Mineralogy and Petrology* **172**, 1–32.

Morgan, G. B. & London, D. (2005). Effect of current density on the electron microprobe analysis of alkali aluminosilicate glasses. *American Mineralogist* **90**, 1131–1138. https://doi.org/10.2138/am.2005.1769.

Murcia, L. A. & Cepeda, H. (1991) *Mapa Geológico de Colombia, Plancha 410 La Unión*. Bogotá: Memoria Explicativa. INGEOMINAS, pp.1–22.

Murri, M., Mazzucchelli, M. L., Campomenosi, N., Korsakov, A. V., Prencipe, M., Mihailova, B. D., Scambelluri, M., Angel, R. J. & Alvaro, M. (2018a). Raman elastic geobarometry for anisotropic mineral inclusions. *American Mineralogist: Journal of Earth and Planetary Materials* **103**, 1869–1872.

Murri, M., Cámara, F., Adam, J., Domeneghetti, M. C. & Alvaro, M. (2018b). Intracrystalline "geothermometry" assessed on clino and orthopyroxene bearing synthetic rocks. *Geochimica et Cosmochimica Acta* **227**, 133–142. https://doi.org/10.1016/j.gca.2018.02.010.

Murri, M., Domeneghetti, M. C., Fioretti, A. M., Nestola, F., Vetere, F., Perugini, D., Pisello, A., Faccenda, M. & Alvaro, M. (2019). Cooling history and emplacement of a pyroxenitic lava as proxy for understanding Martian lava flows. *Scientific Reports* **9**, 17051–17057. https://doi.org/10.1038/s41598-019-53142-0.

Nakamura, D. (2009). A new formulation of garnet–clinopyroxene geothermometer based on accumulation and statistical analysis of a large experimental data set. *Journal of Metamorphic Geology* **27**, 495–508. https://doi.org/10.1111/j.1525-1314.2009.00828.x.

Németh, B., Török, K., Bali, E., Zajacz, Z., Fodor, L. & Szabó, C. (2021). Melt-rock interaction in the lower crust based on silicate melt inclusions in mafic garnet granulite xenoliths, Bakony-Balaton Highland volcanic field (Hungary). *Geologica Carpathica* **72**, 232–252. https://doi.org/10.31577/GeolCarp.72.3.4.

O'Connor, J. T. (1965). A classification for quartz-rich igneous rocks based on feldspar ratios. *United States Geological Survey Professional Paper* **525-B**, 79–84.

Otamendi, J. E., Ducea, M. N. & Bergantz, G. W. (2012). Geological, petrological and geochemical evidence for progressive construction of an arc crustal section, sierra de Valle Fertil, Famatinian arc, Argentina. *Journal of Petrology* **53**, 761–800. https://doi.org/10.1093/petrology/egr079.

Özkan, H., Cartz, L. & Jamieson, J. C. (1974). Elastic constants of nonmetamict zirconium silicate. *Journal of Applied Physics* **45**, 556–562. https://doi.org/10.1063/1.1663283.

Palin, R. M., White, R. W., Green, E. C., Diener, J. F., Powell, R. & Holland, T. J. (2016). High-grade metamorphism and partial melting of basic and intermediate rocks. *Journal of Metamorphic Geology* **34**, 871–892. https://doi.org/10.1111/jmg.12212.

Paton, C., Hellstrom, J., Paul, B., Woodhead, J. & Hergt, J. (2011). Iolite: freeware for the visualisation and processing of mass spectrometric data. *Journal of Analytical Atomic Spectrometry* **26**, 2508–2518. https://doi.org/10.1039/c1ja10172b.

Petrelli, M., Laeger, K. & Perugini, D. (2016a). High spatial resolution trace element determination of geological samples by laser ablation quadrupole plasma mass spectrometry: implications for glass analysis in volcanic products. *Geosciences Journal* **20**, 851–863. https://doi.org/10.1007/s12303-016-0007-z.

Petrelli, M., Morgavi, D., Vetere, F. & Perugini, D. (2016b). Elemental imaging and petro-volcanological applications of an improved laser ablation inductively coupled quadrupole plasma mass spectrometry. *Periodico di Mineralogia* **85**, 25–39. https://doi.org/10.2451/2015PM0465.

Poveda, E., Monsalve, G. & Vargas, C. A. (2015). Receiver functions and crustal structure of the northwestern Andean region, Colombia. *Journal of Geophysical Research: Solid Earth* **120**, 2408–2425. https://doi.org/10.1002/2014JB011304.

Rapp, R. P. & Watson, E. B. (1995). Dehydration melting of metabasalt at 8–32 kbar: implications for continental growth and crust-mantle recycling. *Journal of Petrology* **36**, 891–931. https://doi.org/10.1093/petrology/36.4.891.

Rautela, O., Chapman, A. D., Shields, J. E., Ducea, M. N., Lee, C. T., Jiang, H. & Saleeby, J. (2020). In search for the missing arc root of the Southern California batholith: PTt evolution of upper mantle xenoliths of the Colorado Plateau Transition Zone. *Earth and Planetary Science Letters* **547**, 116447–116413. https://doi.org/10.1016/j.epsl.2020.116447.

Rodríguez-Vargas, A., Koester, E., Mallmann, G., Conceição, R. V., Kawashita, K. & Weber, M. B. I. (2005). Mantle diversity beneath the Colombian Andes, northern volcanic zone: constraints from Sr and Nd isotopes. *Lithos* **82**, 471–484. https://doi.org/10.1016/j.lithos.2004.09.027.

Roedder, E. (1984) Volume 12: fluid inclusions. In: *Reviews in mineralogy* 12. Washington, DC: Mineralogical Society of America, pp. 1–646.

Rosenfeld, J. L. & Chase, A. B. (1961). Pressure and temperature of crystallization from elastic effects around solid inclusions in minerals? *American Journal of Science* **259**, 519–541. https://doi.org/10.2475/ajs.259.7.519.

Rudnick, R. L. (1995). Making continental crust. *Nature* **378**, 571–578. https://doi.org/10.1038/378571a0.

Rudnick, R. L. & Gao, S. (2003) Composition of the continental crust. In: Holland H. D. & Turekian K. K. (eds) *Treatise on Geochemistry*, Vol. 3, 1st edn. Amsterdam: Elsevier, pp.1–64.

Saleeby, J. B. (1990) Progress in tectonic and petrogenetic studies in an exposed cross-section of Young (~100 Ma) Continental Crust, Southern Sierra Nevada, California. In: Salisbury M. H. & Fountain D. M. (eds) *Exposed Cross-Sections of the Continental Crust. NATO ASI Series*, vol 317. Dordrecht: Springer, pp.137–158.

Sawyer, E. W. (2008) Atlas of migmatites. In: *The Canadian Mineralogist Special Publication 9. Quebec: Mineralogical Association of Canada*. Ottawa: Canadian Science Publishing.

Schmidt, M. & Poli, S. (2013) Devolatilization during subduction. In: Holland H. D. & Turekian K. K. (eds) *Treatise on Geochemistry*Vol. 4, 2nd edn. Amsterdam: Elsevier, pp.669–701.

Sen, C. & Dunn, T. (1994). Dehydration melting of a basaltic composition amphibolite at 1.5 and 2.0 GPa: implications for the origin of adakites. *Contributions to Mineralogy and Petrology* **117**, 394–409. https://doi.org/10.1007/BF00307273.

Sheldrick, G. M. (2008). A short history of SHELX. *Acta Crystallographica Section A: Foundations of Crystallography* **64**, 112–122. https://doi.org/10.1107/S0108767307043930.

Stangarone, C., Angel, R. J., Prencipe, M., Campomenosi, N., Mihailova, B. & Alvaro, M. (2019). Measurement of strains in zircon inclusions by Raman spectroscopy. *European Journal of Mineralogy* **31**, 685–694. https://doi.org/10.1127/ejm/2019/0031-2851.

Sudholz, Z. J., Green, D. H., Yaxley, G. M. & Jaques, A. L. (2022). Mantle geothermometry: experimental evaluation and recalibration of Fe–mg geothermometers for garnet-clinopyroxene and garnet-orthopyroxene in peridotite, pyroxenite and eclogite systems. *Contributions to Mineralogy and Petrology* **177**, 1–19. https://doi.org/10.1007/s00410-022-01944-3.

Syracuse, E. M., Maceira, M., Prieto, G. A., Zhang, H. & Ammon, C. J. (2016). Multiple plates subducting beneath Colombia, as illuminated by seismicity and velocity from the joint inversion of seismic and gravity data. *Earth and Planetary Science Letters* **444**, 139–149. https://doi.org/10.1016/j.epsl.2016.03.050.

Taboada, A., Rivera, L. A., Fuenzalida, A., Cisternas, A., Philip, H., Bijwaard, H., Olaya, J. & Rivera, C. (2000). Geodynamics of the northern Andes: subductions and intracontinental deformation (Colombia). *Tectonics* **19**, 787–813. https://doi.org/10.1029/2000TC900004.

Tatsumi, Y. (2000). Continental crust formation by crustal delamination in subduction zones and complementary accumulation of the enriched mantle I component in the mantle. *Geochemistry, Geophysics, Geosystems* **1**, 1–17. https://doi.org/10.1029/2000GC000094.

Taylor, S. R. & McLennan, S. M. (1995). The geochemical evolution of the continental crust. *Reviews of Geophysics* **33**, 241–265. https://doi.org/10.1029/95RG00262.

Triantafyllou, A., Berger, J., Baele, J. M., Bruguier, O., Diot, H., Ennih, N., Monnier, C., Plissart, G., Vandycke, S. & Watlet, A. (2018). Intra-oceanic arc growth driven by magmatic and tectonic processes recorded in the Neoproterozoic Bougmane arc complex (anti-atlas, Morocco). *Precambrian Research* **304**, 39–63. https://doi.org/10.1016/j.precamres.2017.10.022.

Wang, J., Mao, Z., Jiang, F. & Duffy, T. S. (2015). Elasticity of single-crystal quartz to 10 GPa. *Physics and Chemistry of Minerals* **42**, 203–212. https://doi.org/10.1007/s00269-014-0711-z.

Weber, M. B. I. (1998) *The Mercaderes-Río Mayo xenoliths, Colombia: Their bearing on mantle and crustal processes in the Northern Andes*PhD diss. University of Leicester1998, pp.1–295.

Weber, M. B., Tarney, J., Kempton, P. D. & Kent, R. W. (2002). Crustal make-up of the northern Andes: evidence based on deep crustal xenolith suites, Mercaderes, SW Colombia. *Tectonophysics* **345**, 49–82. https://doi.org/10.1016/S0040-1951(01)00206-2.

White, R. W., Powell, R., Holland, T. J. B. & Worley, B. A. (2000). The effect of TiO_2 and Fe_2O_3 on metapelitic assemblages at greenschist and amphibolite facies conditions: mineral equilibria calculations in the system K_2O-FeO-MgO-Al_2O_3-SiO_2-H_2O-TiO_2-Fe_2O_3. *Journal of Metamorphic Geology* **18**, 497–511. https://doi.org/10.1046/j.1525-1314.2000.00269.x.

White, R. W., Powell, R. & Clarke, G. L. (2002). The interpretation of reaction textures in Fe-rich metapelitic granulites of the Musgrave Block, Central Australia: constraints from mineral equilibria calculations in the system K_2O–FeO–MgO–Al_2O_3–SiO_2–H_2O–TiO_2–Fe_2O_3. *Journal of Metamorphic Geology* **20**, 41–55. https://doi.org/10.1046/j.0263-4929.2001.00349.x.

White, R. W., Powell, R., Holland, T. J. B., Johnson, T. E. & Green, E. C. R. (2014). New mineral activity–composition relations for thermodynamic calculations in metapelitic systems. *Journal of Metamorphic Geology* **32**, 261–286. https://doi.org/10.1111/jmg.12071.

Whitney, D. L. & Evans, B. W. (2010). Abbreviations for names of rock-forming minerals. *American Mineralogist* **95**, 185–187. https://doi.org/10.2138/am.2010.3371.

Wolf, M. B. & Wyllie, P. J. (1994). Dehydration-melting of amphibolite at 10 kbar: the effects of temperature and time. *Contributions to Mineralogy and Petrology* **115**, 369–383. https://doi.org/10.1007/BF00320972.

Yanagida, Y., Nakamura, M., Yasuda, A., Kuritani, T., Nakagawa, M. & Yoshida, T. (2018). Differentiation of a hydrous arc magma recorded in melt inclusions in deep crustal cumulate xenoliths from Ichinomegata Maar, NE Japan. *Geochemistry, Geophysics, Geosystems* **19**, 838–864. https://doi.org/10.1002/2017GC007301.

Zeier, M., Hoffmann, J. & Wollensack, M. (2012). Metas.UncLib—A measurement uncertainty calculator for advanced problems. *Metrologia* **49**, 809–815. https://doi.org/10.1088/0026-1394/49/6/809.